# AN ASYMPTOTIC CLOSED-FORM PARAXIAL FORMULATION FOR SURFACE FIELDS ON ELECTRICALLY LARGE DIELECTRIC COATED CIRCULAR CYLINDERS

A THESIS

SUBMITTED TO THE DEPARTMENT OF ELECTRICAL AND

ELECTRONICS ENGINEERING

AND THE INSTITUTE OF ENGINEERING AND SCIENCE

OF BILKENT UNIVERSITY

IN PARTIAL FULFILLMENT OF THE REQUIREMENTS

FOR THE DEGREE OF

MASTER OF SCIENCE

By

Tuncay Erdöl

August, 2005

I certify that I have read this thesis and that in my opinion it is fully adequate, in scope and in quality, as a thesis for the degree of Master of Science.

Assist. Prof. Dr. Vakur B. Ertürk (Advisor)

I certify that I have read this thesis and that in my opinion it is fully adequate, in scope and in quality, as a thesis for the degree of Master of Science.

Prof. Dr. Hitay Özbay

I certify that I have read this thesis and that in my opinion it is fully adequate, in scope and in quality, as a thesis for the degree of Master of Science.

Prof. Dr. Mustafa Kuzuoğlu

Approved for the Institute of Engineering and Science:

Prof. Dr. Mehmet B.Baray
Director of the Institute

# ABSTRACT

## AN ASYMPTOTIC CLOSED-FORM PARAXIAL FORMULATION FOR SURFACE FIELDS ON ELECTRICALLY LARGE DIELECTRIC COATED CIRCULAR CYLINDERS

Tuncay Erdöl
M.S. in Electrical and Electronics Engineering
Supervisor: Assist. Prof. Dr. Vakur B. Ertürk
August, 2005

Investigation of surface fields excited on material coated perfectly conducting (PEC) circular cylinders is a problem of interest (*i*) due to its application in the design and analysis of conformal microstrip antennas and arrays, and (*ii*) it acts as a canonical problem useful toward the development of asymptotic solutions valid for arbitrarily convex material coated smooth surfaces. Nevertheless, integral equation based solutions that use the eigenfunction representation of the appropriate dyadic Green's function, as well as pure numerical solutions become intractable when the geometry of interest is electrically large. A few asymptotic solutions have been suggested in the literature to overcome this problem. However, these solutions are not accurate within the paraxial (nearly axial) region of the cylinder. This is a well known problem that has been observed for PEC and impedance cylinders in the past as well. Recently, a novel paraxial space-domain representation for the surface fields has been presented by Ertürk *et. al.* (*IEEE Trans. Antennas and Propagat.*, 11, 1577-1587, 2002), which is much faster than the well-known eigenfunction solution. However, in this representation the final expressions for the surface fields have some special functions which involve Sommerfeld type integrals to be evaluated numerically.

In this thesis, using the final results of this paraxial space-domain formulation as a starting point, a relatively simple closed-form asymptotic representation for the surface fields of a dielectric coated, electrically large circular cylinder is developed. The large parameter in this asymptotic development is the separation between the source and observation points. The solution uses the fact that

existing special functions in the previously developed paraxial formulation are in similar forms when compared to the special functions used in the Sommerfeld integral representation for the single layer microstrip dyadic Green's function for the planar case. Furthermore, when the radius of the cylinder goes to infinity, using the leading terms of Debye representations for the Hankel and Bessel functions (as well as their derivatives), cylindrical special functions recover their planar counterparts. Therefore, first a steepest descent path representation of these special functions is obtained. Then, using the method suggested by Barkeshli *et. al.* (*IEEE Trans. Antennas and Propagat.*, 9, 1374-1383, 1990) closed-form expressions are achieved.

Numerical results in the form of mutual coupling between two tangential electric current modes have been obtained using these closed-form expressions and compared with the previously developed paraxial formulation as well as eigenfunction solution to assess the accuracy and efficiency of these closed-form solutions. Details of the formulation is presented.

*Keywords:* Coated cylinders, Green's function, asymptotic, paraxial.

# ÖZET

# ELEKTRİKSEL OLARAK BÜYÜK YALITKAN KAPLI METAL SİLİNDİRDEKI YÜZEY DALGALARI İÇİN ASİMPTOTİK KAPALI İFADELER

Tuncay Erdöl
Elektrik ve Elektronik Mühendisliği, Yüksek Lisans
Tez Yöneticisi: Vakur B. Ertürk
Ağustos, 2005

Dielektrik kaplı iletken çembersel silindirlerin üzerinde oluşturulan yüzey dalgalarının incelenmesi iki açıdan önemlidir: (i) Mikroşerit anten ve anten dizilerinin analiz ve tasarımında kullanılmaları, (ii) genel dielektrik kaplı konveks yüzeylerde kullanılabilecek asimptotik metodlar için kanonik bir problem olması. İncelenecek yapının elektriksel büyüklüğü arttıkça, saf ve sayısal çözümler ve Green'in fonksiyonunun özişlev ifadesini kullanan integral tabanlı çözümler kullanılamaz hale gelmektedir. Geçmişte bu problemi çözmek için önerilen asimptotik metodlar da yaklaşık eksensel bölgede doğru sonuçlar vermemektedir. Bu problem iletken ve empedans silindirleri için bilinmektedir. Yaklaşık eksensel bölgedeki yüzey dalgalarının uzamsal bölgede ifadesi Ertürk (*IEEE Trans. Antennas and Propagat.*, 11, 1577-1587, 2002) tarafından verilmiştir. Bu çözüm bilinen özişlev çözümünden daha hızlıdır. Ancak bu çözümde de yüzey dalgaları için bulunan ifadeler Sommerfeld tipi integraller içermektedir. Bu sorunu çözmek için değişik metodlar uygulanmasına rağmen elektriksel olarak büyük problemlerde bu durum sorun çıkarmaktadır.

Bu tezde, yaklaşık eksensel bölgedeki yüzey dalgaları için uzamsal bölge ifadeleri başlangıç noktası olarak seçilip dielektrik kaplı çembersel bir silindirdeki yüzey dalgaları için basit, kapalı asimptotik ifadeler elde edilmiştir. Silindirde yaklaşık eksensel bölgedeki yüzey dalgaları için bulunan ifadeler düzlemsel mikroşeritin Sommerfeld tipi integralle çözümünde bulunan ifadelere benzemektedir. Üstelik silindirin yarıçapı sonsuza gittikçe silindir için bulunan ifadeler düzlem için bulunan ifadelere dönüşmektedir. Buradan hareketle, silindir için

bulunan ifadeleri alıp Barkeshli (*IEEE Trans. Antennas and Propagat.*, 9, 1374-1383, 1990) tarafında önerilen metodla kapalı ifadeler elde edilir.

Silindir üzerindeki silindire teğet iki elektrik akımı arasındaki etkileşim bu tezde elde edilen ifadeler ile, yaklaşık eksensel uzamsal bölge ifadeleri ile ve de özişlev metodu ile çözülüp elde edilen kapalı ifadelerin hassasiyeti ve verimliliği incelenmiştir. Kapalı devre formüllerinin ayrıntıları da verilmiştir.

*Anahtar sözcükler*: Dielektrik kaplı silindirler, Green'in fonksiyonu, asimptotik, yaklaşık eksensel.

*To My Family*

# Acknowledgement

I would like to express my gratitude to my supervisor Assist. Prof. Dr. Vakur B. Ertürk for his instructive comments and continuing support in the supervision of the thesis.

I would like to express my special thanks and gratitude to Prof. Dr. Hitay Özbay and Prof. Dr. Mustafa Kuzuoğlu for showing keen interest to the subject matter and accepting to read and review the thesis.

Finally I would like to thank Aselsan Inc. for letting me to involve in this thesis study and my family for their support.

# Contents

# List of Figures

# Chapter 1

# Introduction

Microstrip structures have been widely used in many areas like satellite and wireless technology, biomedical and remote sensing. They have advantages like low profile, light weight, low cost, compactness, simplicity, versatility, ease of fabrication, and they can conform to any surface providing integration capability to other RF and microwave components. In particular, their ability to conform to any surface makes them very useful in many military and commercial applications. Therefore investigation of surface fields excited on material coated perfectly conducting (PEC) circular cylinders is a problem of interest ($i$) due to its application in the design and analysis of conformal microstrip antennas and arrays for the aforementioned applications, and ($ii$) it acts as a canonical problem useful toward the development of asymptotic solutions valid for arbitrarily convex material coated smooth surfaces.

Many of the existing CAD tools or many researchers have used the radially propagating eigenfunction series representation [1]-[5] for the design and analysis of microstrip structures on coated PEC circular cylinders. However, such a solution is valid only for canonical geometries and exhibit various numerical problems for electrically large cylinders ($r > \lambda_0$; $\lambda_0$ : free space wavelength) and electrically large separations ($s$) between source and observation points. In order to overcome this problem, a few asymptotic solutions have been suggested in the literature [6]-[10]. Munk in [6] derived a UTD-based Green's function representation for

electrically large coated cylinders. His solution includes higher order terms of $1/s$ for the surface fields to make the solution valid even for small separations. However, numerical results showed that only for very thin substrates reasonable results can be obtained for large separations if the leading term is included only [7]. Similar to Munk's work, a steepest descent path (SDP) representation of the dyadic Green's function for dielectric coated circular PEC cylinder is given in [8]. It is based on a circumferentially-propagating series representation of the appropriate Green's function and its numerical evaluation along an SDP on which the integrand decays most rapidly. Numerical results based on this work have showed that in contrast to most asymptotic solutions, the results are valid even for relatively small separations. Furthermore, in the limiting case of large separations, this method reduces to the leading term of [6]. A couple of more studies have been presented in the literature based on the aforementioned works [9]-[10]. However, none of these solutions are accurate along the paraxial (nearly axial) region which is illustrated in Fig. 1.1 (region where $\alpha \rightarrow 90^{\circ}$ ). This is a well-known problem that has been observed for PEC and impedance cylinders in the past [11]-[15]. Among these solutions, Boersma and Lee [14] used a two-term Debye approximation [16] for the logarithmic derivatives of Hankel functions and obtained a closed-form solution for a PEC cylinder (no coating) which remains accurate in the paraxial region. In [17] and [18], a novel space-domain representation for the surface fields excited within the paraxial region of an electrically large dielectric coated circular cylinder is presented. It is based on the fact that the circumferentially-propagating series representation of the Green's function is periodic in one of its variables after an appropriate change of variables is performed. Hence, it can be approximated with a Fourier series (FS) where the coefficients of this series expansion can be easily obtained by a simple numerical integration algorithm. Based on numerical experimentation, it appears that only the two leading terms of the expansion are necessary in most cases. Using this representation, the surface fields are represented by some special functions each of which involves a single Sommerfeld type integral to be evaluated numerically. Certain techniques are implemented to this numerical integration procedure to handle possible singularities of the integrands and to accelerate the integration process. Recently, an asymptotic closed-form solution for the surface magnetic

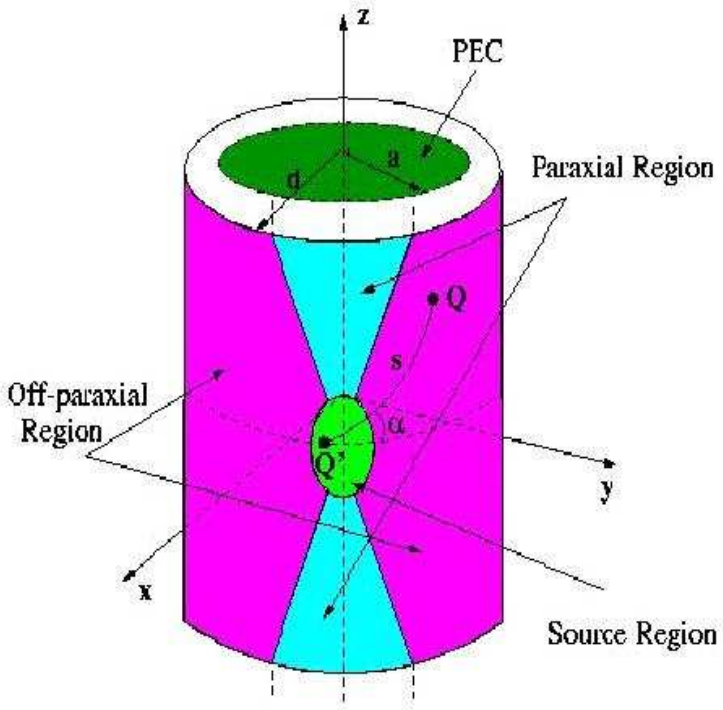


Figure 1.1: Definition of paraxial region.

field within the paraxial region of a circular cylinder with an impedance boundary condition (IBC) is presented in [19]. Similar to the PEC case [14], Hankel functions are asymptotically approximated by a two-term Debye expansion within the spectral integral representation of the relevant Green's function pertaining to the IBC case. One of the two integrals in the resultant spectral representation is evaluated in an exact fashion whereas the second one is evaluated asymptotically.

In this thesis, using the final results of [18] as the starting point, a relatively simple closed-form asymptotic representation for the surface fields of a dielectric coated, electrically large circular cylinder is developed, which is the main contribution of this thesis. The large parameter in this asymptotic development is the separation between the source and observation points in addition to the fact that the cylinder is electrically large ($r > \lambda_0$), which has been made use in arriving the final results of [18]. The solution uses the fact that existing special functions in [18] are in similar forms when compared to the special functions used

in the Sommerfeld integral representation for the single layer microstrip dyadic Green's function for the planar case [20]. Furthermore, using the leading term of Debye representation for the Hankel and Bessel functions (as well as their derivatives), the final expressions given in [18] recover their planar counterparts [20] when the inner and outer radii of the cylinder go to infinity (thickness of the coating remains the same). Therefore, similar to PEC and impedance cylinder cases, two-term Debye expansions are used for all cylindrical special functions [10]. It should be noted that the expressions for PEC and impedance cylinders are significantly simpler than the expressions for material coated cylinders. Furthermore, they involve only Hankel function and its derivative, whereas in coated cylinders, there exists a combination of Hankel and Bessel functions along with their derivatives (we call it cylindrical functions). Therefore, the two-term Debye expressions derived by Marin [10] are complicated and possess some restrictions to our solution range. Once the final expressions are obtained for the integrands of the final results of [18] using the two-term Debye approximations, the method used in [20] is applied. The final closed-form expressions involve only trigonometric and polynomial terms. Although they are asymptotic expressions with respect to the separation between source and observation points, they work even for relatively small separations for some cases.

In Chapter 2, a brief review of [20] is presented. It summarizes the method to obtain the asymptotic expression and its usage for planar microstrip surface which is a special case of the cylinder problem. Chapter 3 summarizes [18], the result of which is the starting point for this thesis. In Chapter 4 asymptotic expressions are obtained for the dielectric coated circular PEC cylinder. In chapter 5, numerical results and comparisons with the eigenfunction and FS solutions are given. Chapter 6 summarizes our results and gives a brief conclusion for this thesis. There are also three appendices in this thesis. Appendix A gives the explicit expressions for the residues of the planar functions. Appendix B gives the explicit expressions for the parameters $f_{a0_Y}(d)$ and $f_{a2_Y}(d)$, which are very important for the final form of our closed-form representations. Appendix C gives the explicit expressions for the residues of the special functions used for the asymptotic closed-form expressions developed in Chapter 4. Note that an $e^{j\omega t}$

time convention is used and suppressed throughout this thesis, where $\omega = 2\pi f$ is the angular frequency, $j = \sqrt{-1}$ and $t$ is time.

# Chapter 2

# Development of an Asymptotic Closed-Form Expression for Planar Microstrip Structure

## 2.1 Introduction

A special case for the problem of dielectric coated circular cylinder is a microstrip planar surface when the radius of the cylinder goes to infinity. Development of an asymptotic closed-form expression for planar microstrip surface Green's function is investigated in [20]. The large parameter for this asymptotic expression is the separation between the source and observation points in terms of wavelength. Since the method in achieving the asymptotic closed-form paraxial formulation for surface fields on electrically large dielectric coated circular cylinders is based on the method developed in [20], a review of [20] is given here. The notation used in this chapter is similar to that of [20].

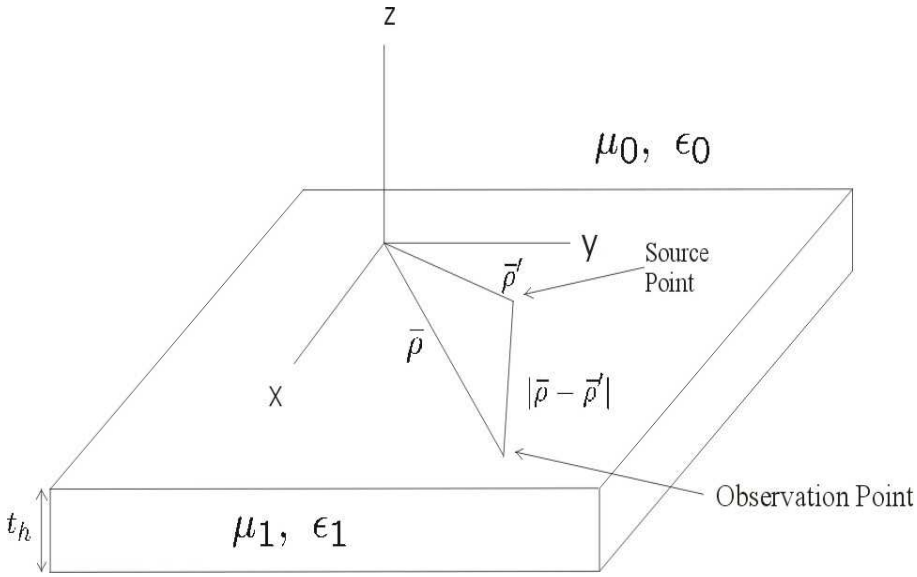


Figure 2.1: Microstrip Planar Structure

## 2.2 Formulation

For an arbitrarily oriented electric current source $\bar{J}(r)$ on a grounded dielectric slab as shown in the Fig. 2.1, the corresponding electric field $\bar{E}_m$ is given by

$$\bar{E}_m = -j\omega\mu_0 \int\int_v \int \bar{\bar{G}}^m(\bar{r},\bar{r}') \cdot \bar{J}(\bar{r}')dv' \tag{2.1}$$

where $\bar{\bar{G}}^m(r,r')$ is the microstrip dyadic Green's function. Here $m = 0$ refers to the case when the observation point is in free space and $m = 1$ refers to the case when the observation point is in the dielectric slab with constitutive parameters $\epsilon_1$ and $\mu_1$. If the electric current source is a point source with strength $p_e$ at $\bar{r} = \bar{r}'$

$$\bar{J}(\bar{r}') = \bar{p}_e\delta(\bar{r}-\bar{r}'), \tag{2.2}$$

where $\delta(\bar{r}-\bar{r}')$ is the Dirac delta function, the electric field produced by it is given as

$$\bar{E}_m = -j\omega\mu_0 \bar{\bar{G}}^m(\bar{r}, \bar{r}') \cdot \bar{p}_e. \tag{2.3}$$

Assuming that the point source is located at the dielectric-air interface at $z = 0$ and oriented transverse to $\hat{z}$ (i.e. parallel to the plane of the dielectric slab), the matrix form of (2.3) is given by

$$\begin{bmatrix} E_{mx} \\ E_{my} \\ E_{mz} \end{bmatrix} = -j\omega\mu_0 \begin{bmatrix} G^m_{xx} & G^m_{xy} & G^m_{xz} \\ G^m_{yx} & G^m_{yy} & G^m_{yz} \\ G^m_{zx} & G^m_{zy} & G^m_{zz} \end{bmatrix} \begin{bmatrix} p_{ex} \\ p_{ey} \\ 0 \end{bmatrix} \tag{2.4}$$

where $p_{ex}$ and $p_{ey}$ are the $x$ and $y$ components of $\bar{p}_e$ respectively ($z$ component of current is assumed to be zero ). For observation points in free-space (m=0) and the source point is at the origin, the Green's function components of $\bar{\bar{G}}^m$ (with $m = 0$) in (2.4) are obtained as

$$G^0_{xx}(\bar{r}, 0) = \frac{-j}{2\pi k_0^2} \left\{ k_0^2 U + \frac{\partial^2}{\partial x^2} \left( U - \frac{\epsilon_r - 1}{\epsilon_r} W \right) \right\} \tag{2.5}$$

$$G^0_{yx}(\bar{r}, 0) = \frac{-j}{2\pi k_0^2} \left\{ \frac{\partial^2}{\partial x \partial y} \left( U - \frac{\epsilon_r - 1}{\epsilon_r} W \right) \right\} \tag{2.6}$$

$$G^0_{zx}(\bar{r}, 0) = \frac{j}{2\pi k_0^2} \left\{ \frac{\partial}{\partial x}(V) \right\} \tag{2.7}$$

$$G^0_{xy}(\bar{r}, 0) = G^0_{yx}(\bar{r}, 0) \tag{2.8}$$

$$G^0_{yy}(\bar{r}, 0) = \frac{-j}{2\pi k_0^2} \left\{ k_0^2 U + \frac{\partial^2}{\partial y^2} \left( U - \frac{\epsilon_r - 1}{\epsilon_r} W \right) \right\} \tag{2.9}$$

$$G^0_{zy}(\bar{r}, 0) = \frac{j}{2\pi k_0^2} \left\{ \frac{\partial}{\partial y}(V) \right\} \tag{2.10}$$

with $k_0 = \omega\sqrt{\mu_0\epsilon_0}$. In (2.5)-(2.10), the Green's function components are written in terms of three special functions $U$, $V$ and $W$. These special functions are expressed in Sommerfeld ($z$-propagation) representation as:

$$U = \frac{1}{2}\int_{-\infty}^{\infty}\frac{\xi e^{-jK_0(\xi)z}}{K_0(\xi)+Y(\xi)}H_0^{(2)}(\rho\xi)d\xi \tag{2.11}$$

$$W = \frac{1}{2}\int_{-\infty}^{\infty}\frac{\xi Z(\xi)e^{-jK_0(\xi)z}}{K_0(\xi)+Z(\xi)}H_0^{(2)}(\rho\xi)d\xi \tag{2.12}$$

$$V = \frac{1}{2}\int_{-\infty}^{\infty}\frac{\xi K_0(\xi)e^{-jK_0(\xi)z}}{(K_0(\xi)+Y(\xi))(K_0(\xi)+Z(\xi))}H_0^{(2)}(\rho\xi)d\xi \tag{2.13}$$

where

$$Z(\xi) = j\frac{K_1(\xi)}{\epsilon_r}tan(K_1(\xi)t_h) \tag{2.14}$$

$$Y(\xi) = -jK_1(\xi)cot(K_1(\xi)t_h) \tag{2.15}$$

$$K_0(\xi) = \sqrt{k_0^2-\xi^2}; \quad K_1(\xi) = \sqrt{\epsilon_r k_0^2-\xi^2} \tag{2.16}$$

$$k_0^2 = \omega^2\mu_0\epsilon_0; \quad \epsilon_r = \frac{\epsilon_1}{\epsilon_0}. \tag{2.17}$$

Finally, in (2.11)-(2.13) $\rho = |\bar{\rho}-\bar{\rho}'|$ is the lateral separation between the source and observation points. These special functions can be written in radially-propagating representation by deforming the sommerfeld integration contour such a way that all relevant singularities including the surface wave poles and branch cuts in the lower half-plane are enclosed as shown in Fig. 2.2. The integration around the branch cut can be transformed to a real-axis integration by the transformation,

$$\zeta = \sqrt{k_0^2-\xi^2} \;\; ; \;\; d\xi = \frac{-\zeta d\zeta}{\sqrt{k_0^2-\zeta^2}} \tag{2.18}$$

and the alternative radially propagating representations for $U$, $V$ and $W$ are obtained as

$$U = \frac{1}{2}\left[\int_{-\infty}^{\infty}\frac{\zeta\; e^{-j\zeta z}}{\zeta \;+\; Y(\zeta)}H_0^{(2)}(\rho\sqrt{k_0^2-\zeta^2})\; d\zeta\right] - 2\pi j\sum_{n''}Res_U(\zeta_{n''}) \tag{2.19}$$

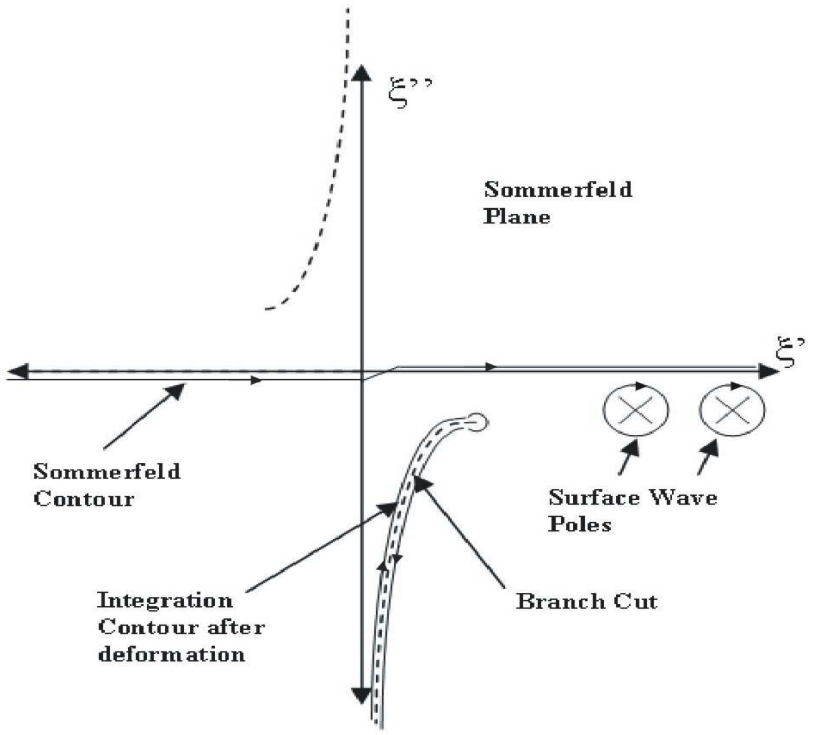


Figure 2.2: Integration contours and branch cuts

$$V = \frac{1}{2}\left[\int_{-\infty}^{\infty} \frac{Z(\zeta)\ \zeta e^{-j\zeta z}}{\zeta + Z(\zeta)} H_0^{(2)}(\rho\sqrt{k_0^2-\zeta^2})\ d\zeta\right] - 2\pi j \sum_{n'} Res_V(\zeta_{n'}) \qquad (2.20)$$

$$W = \frac{1}{2}\left[\int_{-\infty}^{\infty} \frac{\zeta^2\ e^{-j\zeta z}}{(\zeta + Y(\zeta))(\zeta + Z(\zeta))} H_0^{(2)}(\rho\sqrt{k_0^2-\zeta^2})\ d\zeta\right]$$

$$-2\pi j \sum_{n''} Res_W(\zeta_{n''}) - 2\pi j \sum_{n'} Res_W(\zeta_{n'}). \qquad (2.21)$$

In these formulations (2.19)-(2.21), $Res_U(\zeta_{n''})$, $Res_V(\zeta_{n'})$, $Res_W(\zeta_{n'})$ and $Res_W(\zeta_{n''})$ are the residues of the poles in the integrands of $U$, $V$ and $W$ functions. These poles are the ones we captured when we deformed the Sommerfeld integration contour to the contour around the branch-cut. They are all placed in lower half part of $\zeta$-plane after the transformation, so they are all proper transverse electric (TE) or transverse magnetic (TM) surface wave poles ($\zeta_n''$ and $\zeta_n'$, respectively). Leaky wave poles do not contribute directly at this stage.

This radially propagating integral representation of the Green's function converges rapidly for laterally separated source and observation points, because for $\zeta > k_0$ Hankel function decays exponentially. Asymptotic closed-form expressions for large separations can be obtained from these radially propagating representations by the following method:

All special functions $U$, $V$ and $W$ have the same mathematical form. Therefore, consider the integral $I$, which has the following functional form:

$$I = \int_{-\infty}^{\infty} F(\zeta)\, e^{-j\zeta z}\, H_0^{(2)}\left(\rho\sqrt{k_0^2-\zeta^2}\right)\, d\zeta, \tag{2.22}$$

where $F(\zeta)$ function represents the integrands of $U$, $V$ or $W$ functions. Assuming that $F(\zeta)$ has finite number of poles (leaky or surface poles) at $\zeta_p$ close to $\zeta = 0$, one can write

$$F(\zeta) = \sum_n a_n \zeta^n + \sum_p \frac{R_F(\zeta_p)}{\zeta - \zeta_p}. \tag{2.23}$$

In (2.23) $R_F(\zeta_p)$ is the residue of $F(\zeta)$ at $\zeta = \zeta_p$, and $a_n$ are the coefficients of the power series. Substituting (2.23) into (2.22) and introducing the following change of variables

$$\zeta = k_0\eta \;\; ; \;\; d\zeta = k_0 d\eta \;\; ; \;\; \eta_p = \zeta_p/k_0 \tag{2.24}$$

the integral $I$ can be obtained as

$$I = k_0 \sum_n \frac{a_n}{(-j)^n}\frac{\partial}{\partial\rho^n}\int_{-\infty}^{\infty} H_0^{(2)}\left(k_0\rho\sqrt{1-\eta^2}\right) e^{-jk_0\eta z} d\eta$$

$$+ \sum_p R_F(\zeta_p)\int_{-\infty}^{\infty} \frac{H_0^{(2)}\left(k_0\rho\sqrt{1-\eta^2}\right)}{\eta-\eta_p} e^{-jk_0\eta z} d\eta. \tag{2.25}$$

The first integral in (2.25) can be evaluated in closed-form. Thus, denoting this integral by $I_0$, it is obtained as

$$\begin{aligned} I_0 &= \int_{-\infty}^{\infty} H_0^{(2)}(k_0\rho\sqrt{1-\eta^2}) e^{-jk_0\eta z} d\eta \\ &= 2j\frac{e^{-jk_0\sqrt{z^2+\rho^2}}}{k_0\sqrt{z^2+\rho^2}}. \end{aligned} \tag{2.26}$$

The second integral in (2.25) is denoted by $I_s$ and asymptotically obtained as

$$I_s \approx \sqrt{\frac{2}{\pi k_0 \rho}} e^{j\pi/4} \int_{-\infty}^{\infty} \frac{1}{(\sqrt{1-\eta^2})^{1/2}} \left(1 + \frac{j}{8k_0\rho(\sqrt{1-\eta^2})}\right) \cdot \frac{e^{-jk_0(\rho\sqrt{1-\eta^2}+\eta z)}}{\eta - \eta_p} d\eta \tag{2.27}$$

by using the large argument approximation of the Hankel function given by

$$H_0^{(2)}(x) \approx \sqrt{\frac{2}{\pi x}} e^{j\pi/4} e^{-jx} \left(1 + \frac{j}{8x}\right). \tag{2.28}$$

Note that in (2.27) due to $\sqrt{1-\eta^2}$ term, the integrand has branch points at $\eta = \pm 1$. Therefore, the branch which satisfies $Im(\sqrt{1-\eta^2}) < 0$ on the entire top sheet of $\eta$-plane is selected. Next step is to continue with (2.27) to obtain a closed-form expression. Therefore, first an angular spectrum mapping

$$\eta = cos\gamma \;\; ; \;\; d\eta = -sin\gamma \; d\gamma \;\; ; \;\; \gamma_p = cos^{-1}(\eta_p) \tag{2.29}$$

is introduced into (2.27) so that the two-sheeted complex $\eta$ plane shown in Fig 2.3 can be mapped into various adjacent sections of width $2\pi$ in the complex $\gamma$ plane ($-\pi/2 \leq Re\ \gamma \leq 3\pi/2$) as shown in Fig 2.4. As a result (2.27) becomes

$$I_s \approx \sqrt{\frac{2}{\pi k_0 r\ sin\ \theta}} e^{j\pi/4} \int_{\Gamma} \left(1 + \frac{j}{8k_0 r\ sin\ \theta\ sin\ \gamma}\right) \frac{1}{\sqrt{sin\ \gamma}} \cdot \frac{e^{-jk_0 r\ cos\ (\theta-\gamma)}}{cos\gamma - cos\gamma_p}\ sin\ \gamma\ d\gamma \tag{2.30}$$

where $\Gamma$ is the path of integration in the complex $\gamma$ plane as shown in Fig 2.4. Note that the polar transformations

$$\rho \;=\; r\ sin\ \theta \;\; ; \;\; z \;=\; r\ cos\ \theta \tag{2.31}$$

are also utilized to reach (2.30).

As the next step $\Gamma$ contour is deformed into the steepest descent path $\Gamma_{SDP}$, then, the contour $\Gamma_{SDP}$ is mapped onto the real axis of the $s$-plane [20], [22], [23]. Consequently (2.30) is written in terms of the SDP integral plus the residue

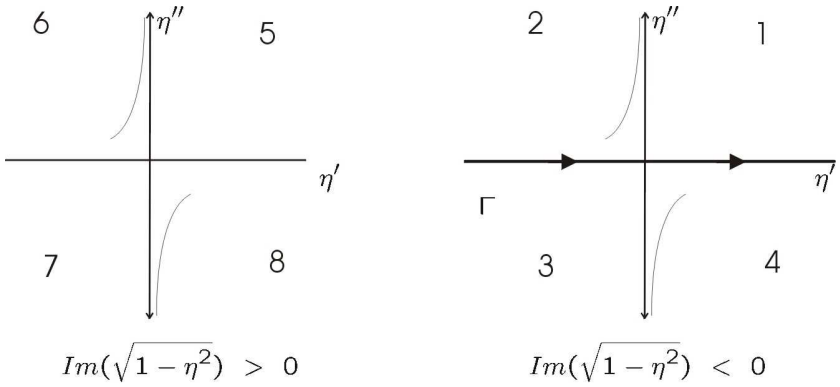


Figure 2.3: Two sheeted $\eta$-plane and integration path for (2.27).

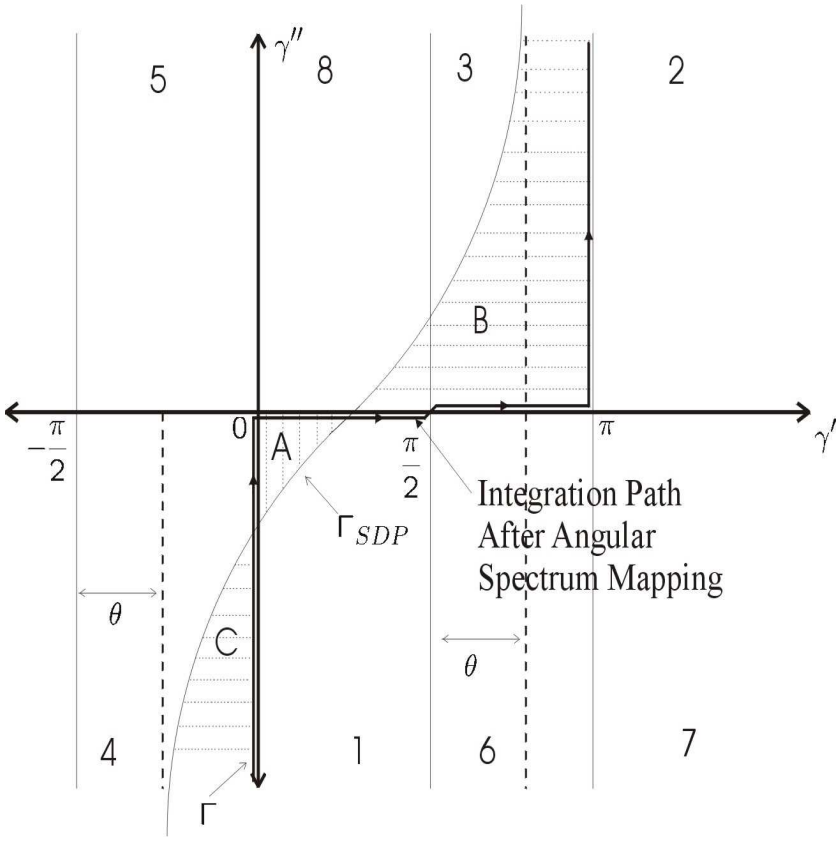


Figure 2.4: Angular Spectrum Mapping. Numbers show that which region of two-sheeted $\eta$-plane map to which region of $\gamma$-plane. Integration paths after angular spectrum mapping and deformation to SDP are also shown.

contribution of the poles which may be captured during the path deformation and given by

$$I_s \approx 2\pi j N(\eta_p) H_0^{(2)}(k_0\rho\sqrt{1-\eta_p^2}) e^{-jk_0\eta_p z} + \sqrt{\frac{2}{\pi\ k_0\ \rho}} e^{j\pi/4} e^{-jk_0 r} \int_{-\infty}^{\infty} G(s) e^{-k_0 r s^2} ds \tag{2.32}$$

where

$$G(s) = \left(1 + \frac{j}{8k_0\rho\ sin\ \gamma}\right) \frac{\sqrt{sin\ \gamma}}{cos\ \gamma\ -\ cos\ \gamma_p} \frac{d\gamma}{ds} \tag{2.33}$$

and

$$N(\eta_p) = \begin{cases} 1 & \text{if pole } (\gamma_p) \text{ is in regions B or C} \\ -1 & \text{if pole } (\gamma_p) \text{ is in regions A} \\ 0 & \text{if pole } (\gamma_p) \text{ is not captured during deformation} \end{cases} \tag{2.34}$$

where regions A, B and C are defined in Figure 2.4.

Finally, the leading term of the uniform asymptotic expansion of (2.32) for $k_0 r \gg 1$ is written [20], [22] as

$$I_s \approx M(k_0 r, \eta_{p_w}) = 2\pi j N(\eta_p) H_0^{(2)}(k_0\rho\ sin\ \gamma_p) e^{-jk_0 z\ cos\ \gamma_p} + 2j\ \frac{e^{-jk_0 r}}{k_0 r}\ \left(1 + \frac{j}{8k_0 r\ sin^2\theta}\right) \left[\frac{1}{cos\ \theta - cos\ \gamma_p} - \frac{1}{2\sqrt{sin\theta}\sqrt{sin\ \gamma_p}\ sin\left(\frac{\gamma_p - \theta}{2}\right)} \left(1 - F\left(2k_0\ r\ sin^2\left(\frac{\gamma_p - \theta}{2}\right)\right)\right)\right] \tag{2.35}$$

where

$$F(x) = 2j\sqrt{x} e^{jx} \int_{\sqrt{x}}^{\infty} e^{-ju^2}\ du \tag{2.36}$$

is the transition function [23] (or [20]) and the positive branch of $\sqrt{sin\gamma_p}$ is used.

When both the source and observation points are located at the dielectric-air interface of Fig. 2.1 (both lie on the substrate, $z = 0$), the uniform asymptotic

approximation of $I$ given by (2.25) can be written as

$$I \approx k_0 a_0 I_0 + k_0^3 a_2 I_2 + \sum_p R_F(\zeta_p) M(k_0\rho, \eta_p) \tag{2.37}$$

where

$$I_0 \;=\; \int_{-\infty}^{\infty} H_0^{(2)}(k_0\rho\sqrt{1-\eta^2}) e^{-jk_0\eta z} d\eta \,\Big|_{z=0} \;=\; 2j\frac{e^{-jk_0\rho}}{k_0\rho} \tag{2.38}$$

$$I_2 \;=\; \int_{-\infty}^{\infty} H_0^{(2)}(k_0\rho\sqrt{1-\eta^2}) e^{-jk_0\eta z}\eta^2 \; d\eta \,\Big|_{z=0} = \; \frac{-2e^{-jk_0\rho}}{(k_0\rho)^2}\left(1+\frac{1}{jk_0\rho}\right) \tag{2.39}$$

and $M(k_0\rho, \eta_p)$ is given by

$$\begin{aligned} M(k_0\rho,\eta_p) \;=\; & -2\pi j N(\eta_p) H_0^{(2)}(k_0\rho\sqrt{1-\eta_p^2}) - 2j\;\frac{e^{-jk_0\rho}}{k_0\rho\eta_p}\;\left(1+\frac{j}{8k_0\rho}\right) \\ & \cdot\left[1+\frac{\eta_p}{2\sqrt{sin\gamma_p}\;sin(\frac{\gamma_p}{2}-\frac{\pi}{4})}\right. \\ & \left.\left(1-F\left(2k_0\;\rho\;sin^2(\frac{\gamma_p}{2}-\frac{\pi}{4})\right)\right)\right]. \end{aligned} \tag{2.40}$$

For lossless media, the proper and improper surface wave poles [21] lie on the imaginary axis of $\eta$ plane. Therefore, for the poles

$$\eta_p \;=\; \pm j|\eta_p| \begin{cases} (-) & \text{for proper surface wave} \\ (+) & \text{for improper surface wave} \end{cases} \tag{2.41}$$

and the corresponding value of $\gamma_p$ becomes

$$\gamma_p \;=\; cos^{-1}(\eta_p) \;=\; \frac{\pi}{2} \pm j\gamma_p'' \begin{cases} (+) & \text{for proper surface wave} \\ (-) & \text{for improper surface wave} \end{cases} \tag{2.42}$$

and hence, the expression for $sin(\gamma_p/2 - \pi/4)$ is expressed as

$$sin\left(\frac{\gamma_p}{2}-\frac{\pi}{4}\right) \;=\; \pm\frac{j}{\sqrt{2}}\sqrt{\sqrt{1+|\eta_p|^2}-1} \begin{cases} (+) & \text{for proper surface wave} \\ (-) & \text{for improper surface wave.} \end{cases} \tag{2.43}$$

Consequently, the uniform asymptotic approximation of $U$, $V$ and $W$ are given by

$$\begin{aligned} U &= \left[\sum_{p_u}\left(\frac{R_U(\zeta_{p_u})}{\zeta_{p_u}}\right)k_0 I_0 \right. \\ &\quad + \left(-\frac{1}{2Y^2(0)} + \sum_{p_u}\frac{R_U(\zeta_{p_u})}{(\zeta_{p_u})^3}\right)k_0^3 I_2 \\ &\quad \left. + \sum_{p_u} R_U(\zeta_{p_u}) M(k_0\rho, \eta_{p_u}) - 2\pi j \sum_{n''} Res_U(\zeta_{n''})\right] \end{aligned} \tag{2.44}$$

$$\begin{aligned} V &= \left[\sum_{p_v}\left(\frac{R_V(\zeta_{p_v})}{\zeta_{p_v}}\right)k_0 I_0 \right. \\ &\quad + \left(\frac{j}{2Z(0)} + \sum_{p_v}\frac{R_V(\zeta_{p_v})}{(\zeta_{p_u})^3}\right)k_0^3 I_2 \\ &\quad \left. + \sum_{p_v} R_V(\zeta_{p_v}) M(k_0\rho, \eta_{p_v}) - 2\pi j \sum_{n'} Res_V(\zeta_{n'})\right] \end{aligned} \tag{2.45}$$

$$\begin{aligned} W &= \left[\sum_{p_w}\left(\frac{R_W(\zeta_{p_w})}{\zeta_{p_w}}\right)k_0 I_0 \right. \\ &\quad + \left(\frac{\epsilon_r}{2k_0^2(\epsilon_r - 1)} + \sum_{p_w}\frac{R_W(\zeta_{p_w})}{(\zeta_{p_w})^3}\right)k_0^3 I_2 \\ &\quad + \sum_{p_w} R_W(\zeta_{p_w}) M(k_0\rho, \eta_{p_w}) - 2\pi j \sum_{n''} Res_W(\zeta_{n''}) \\ &\quad \left. -2\pi j \sum_{n'} Res_W(\zeta_{n'})\right] \end{aligned} \tag{2.46}$$

where

$$Y(0) = -jk_0\sqrt{\epsilon_r - 1}\; cot(k_0 t_h \sqrt{\epsilon_r - 1}) \tag{2.47}$$

$$Z(0) = jk_0\frac{\sqrt{\epsilon_r - 1}}{\epsilon_r}\; tan(k_0 t_h \sqrt{\epsilon_r - 1}). \tag{2.48}$$

In the $U$, $V$ and $W$ expressions $I_0$, $I_2$ and $M(k_0\rho, \eta_p)$ are given in (2.38), (2.39) and (2.40), respectively. $R_T(\zeta_p)$, $(T = U,\ V,\ W)$ are associated with the residues

$\mathrm{Res}_T(\zeta_p)$ of the surface wave or leaky wave poles in the integrands of $U$, $V$ and $W$, respectively, and given by

$$\mathrm{Res}_{T(\zeta_p)} = -R_{T(\zeta_p)} H_0^{(2)}(\rho \sqrt{k_0^2 - \zeta_p^2}) e^{-j\zeta_p z}, \tag{2.49}$$

where the explicit expressions for $R_{T(\zeta_p)}$ are given in Appendix A. Note that only the transition effects of the surface wave poles which are in the vicinity of the saddle point, and one leaky wave pole are included. Furthermore, when both the source and observation points are on the substrate ($z$=0), the first term of (2.40) which involve $N(\eta_p)$ is zero.

In arriving the above expressions (2.44), (2.45), (2.46) a power series expansion around $\zeta = 0$ for the integrands of $U$, $V$ ,$W$ (excluding the factor $H_0^{(2)}(\rho \sqrt{k_0^2 - \zeta_p^2}) e^{-j\zeta_p z}$) is performed as

$$\frac{\zeta}{\zeta + Y(\zeta)} \simeq \frac{\zeta}{Y(0)} \left(1 - \frac{\zeta}{Y(0)} + 0(\zeta^2) + \dots \right) \tag{2.50}$$

$$\frac{\zeta Z(\zeta)}{\zeta + Z(\zeta)} \simeq \zeta \left(1 - \frac{\zeta}{Y(0)} + 0(\zeta^2) + \dots \right) \tag{2.51}$$

$$\frac{\zeta^2}{(\zeta + Y(\zeta))(\zeta + Z(\zeta))} \simeq \zeta^2 \left(\frac{\epsilon_r}{k_0^2(\epsilon_r - 1)} + 0(\zeta^3) + \dots \right) \tag{2.52}$$

and

$$\frac{\mathrm{Res}_F(\zeta_p)}{\zeta - \zeta_p} = -\frac{\mathrm{Res}_F(\zeta_p)}{\zeta_p} \left(1 + \frac{\zeta}{\zeta_p} + \frac{\zeta^2}{\zeta_p^2} + ... \right). \tag{2.53}$$

## 2.3 Numerical Results

In this section a few numerical results are given to show the accuracy of this asymptotic approach compared to the standard eigenfunction solution. To test the accuracy, mutual impedance between two tangential current components are calculated. In numerical calculations, the parameters of planar microstrip are dielectric thickness $t_h = 0.06\lambda_0$, $\epsilon_r = 3.25$ ($\lambda_0$ = free-space wavelength). Note that the mutual impedance $Z_{nm}$ between the current modes is simply given by

$$Z_{nm} = \int_{S_m} \mathbf{E}_n \cdot \mathbf{J}_m \, ds \tag{2.54}$$

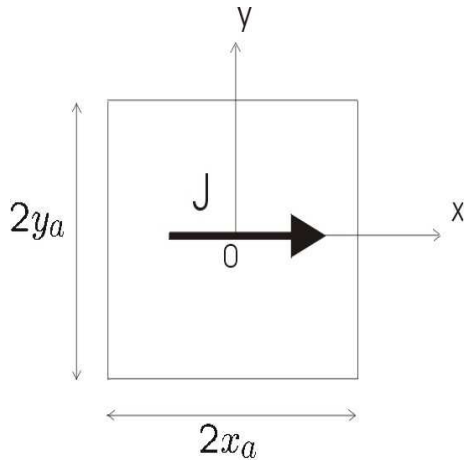


Figure 2.5: Geometry for definition of piecewise sinusoidal current distribution

where $\mathbf{E}_n$ is the field due to source (current mode) $\mathbf{J}_n$ and $S_m$ is the area occupied by source (current mode) $\mathbf{J}_m$. The current modes are defined by a piecewise sinusoid along the direction of the current and they are constant along the direction perpendicular to the current. The expression for such a piecewise sinusoidal current in the $x$-direction is given by

$$J(x) \;=\; \begin{cases} \frac{sin(k_a(x_a-|x|))}{2y_a\ sin(k_a x_a)} & |x| < x_a \\ 0 & elsewhere \end{cases} \tag{2.55}$$

where $k_a = k_0\sqrt{(\epsilon_r+1)/2}$, and $x_a$ and $y_a$ are illustrated in Fig. 2.5.

Each element has dimensions of $0.05\lambda_0$ (along the direction of the current) by $0.02\lambda_0$. In Figures 2.6 and 2.7, the real and imaginary parts of $Z_{xx}$ (Coupling between two $\hat{x}$-directed dipoles) is plotted against separation, by this method (closed-form asymptotic) and compared with the eigenfunction solution given by [24]. The dipoles are placed along the $x$-axis. Similarly, in Figures 2.8 and 2.9, the real and imaginary parts of $Z_{xx}$ is plotted against separation, for the case when the dipoles are placed along the $y$-axis, and again compared with the eigenfunction solution.

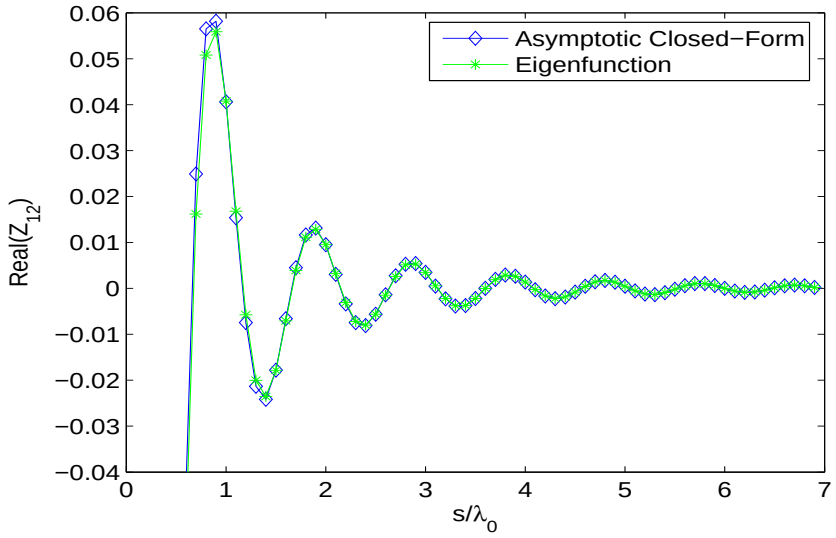


Figure 2.6: Real part of the mutual impedance ($Z_{12}$) between two identical $\hat{x}-$directed current sources versus separation $s$ when $\alpha = 90^\circ$ for a planar microstrip structure with $t_h = 0.06\lambda_0$, $\epsilon_r = 3.25$

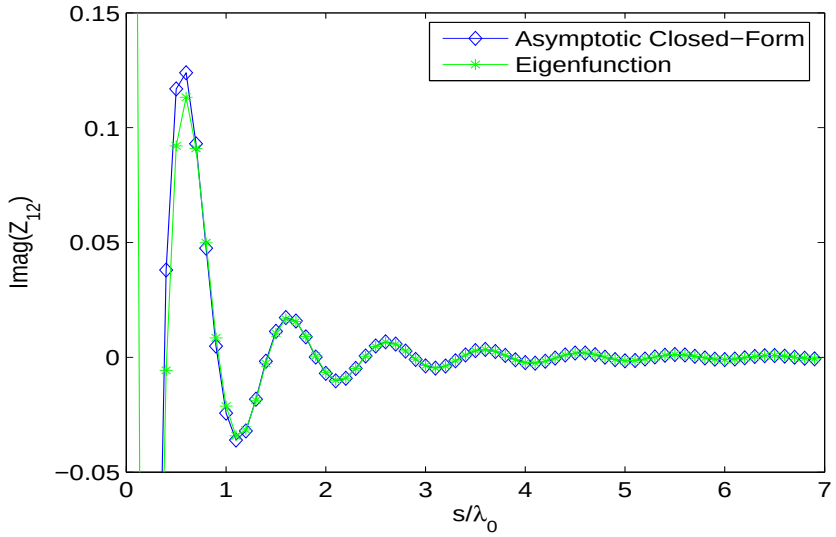


Figure 2.7: Imaginary part of the mutual impedance ($Z_{12}$) between two identical $\hat{x}-$directed current sources versus separation $s$ when $\alpha = 90^\circ$ for a planar microstrip structure with $t_h = 0.06\lambda_0$, $\epsilon_r = 3.25$

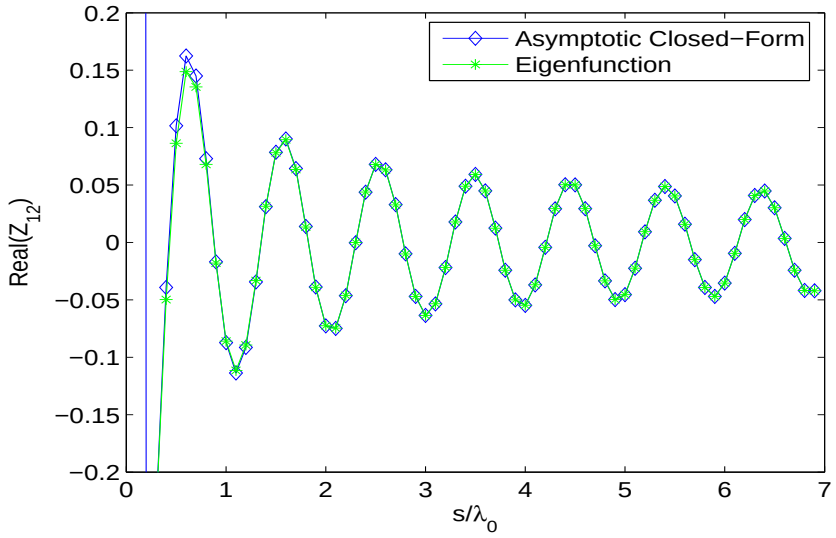


Figure 2.8: Real part of the mutual impedance ($Z_{12}$) between two identical $\hat{x}-$directed current sources versus separation $s$ when $\alpha = 0°$ for a planar microstrip structure with $t_h = 0.06\lambda_0$, $\epsilon_r = 3.25$

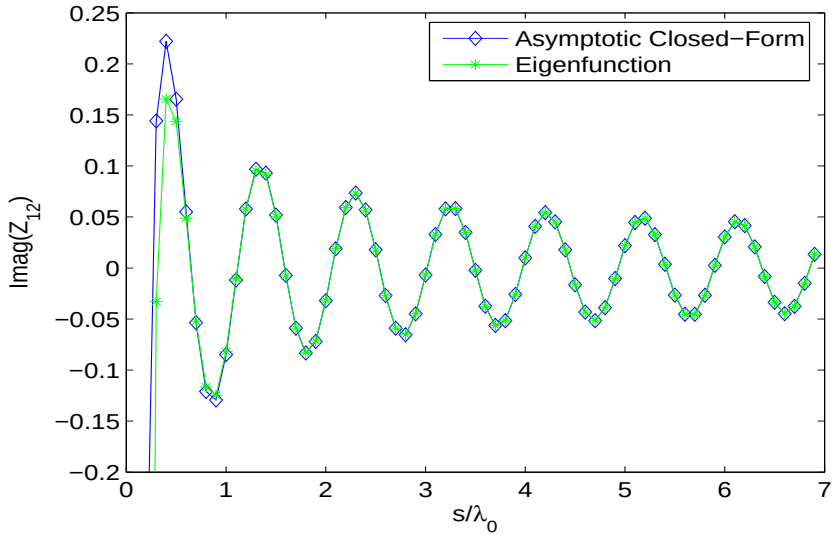


Figure 2.9: Imaginary part of the mutual impedance ($Z_{12}$) between two identical $\hat{x}-$directed current sources versus separation $s$ when $\alpha = 0°$ for a planar microstrip structure with $t_h = 0.06\lambda_0$, $\epsilon_r = 3.25$

As seen in all plots, excellent agreement is observed between the closed-form asymptotic solutions and the eigenfunction solution even for relatively small separations. On the other hand these closed-form asymptotic solutions are approximately 200 times faster than the eigenfunction solution.

# Chapter 3

# Paraxial Space-Domain Formulation for Surface Fields on a Large Dielectric Coated Circular Cylinder

## 3.1 Introduction

As mentioned at the introduction part, a paraxial spatial domain representation of the dyadic Green's function is developed for an electrically large dielectric coated circular cylinder in [17], [18], to obtain the corresponding surface fields accurately along the paraxial region. Since the final results of [17] is the starting point for the asymptotic closed-form expressions (which is the main purpose and contribution of this thesis) developed in the following chapter, the work done in [17] and [18] is briefly reviewed in this chapter. A similar notation to those of [17] and [18] is used.

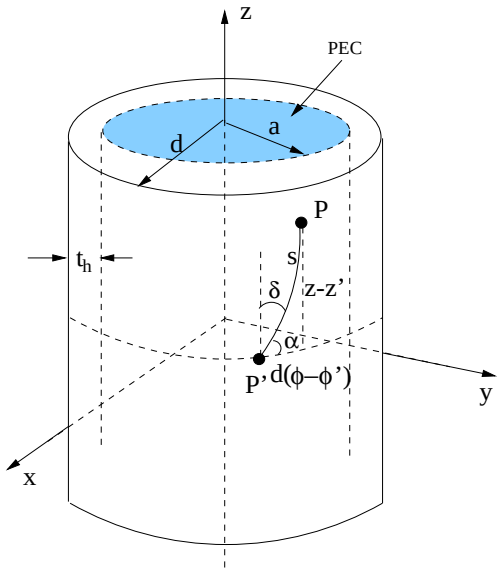


Figure 3.1: Dielectric coated perfect electric conducting (PEC) circular cylinder where the radius of the PEC cylinder is $a$ and the thickness of the dielectric coating is $t_h = d - a$

## 3.2 Formulation

Consider an elementary surface electric current source given by

$$J_e = (P_e^z \hat{z} + P_e^\phi \hat{\phi}) \frac{\delta(\phi - \phi')\delta(z - z')}{d} \tag{3.1}$$

located on the surface of a dielectric coated circular cylinder whose geometry is given in Fig. 3.1 ($\rho = \rho' = d$). The surface field component in the $l$-direction ($l = \phi$ or $z$) at $\rho = d$ excited by a $u$-directed source defined in (3.1) ($u = \phi$ or $z$) can be written as

$$E_l(z, \phi) = \frac{1}{2\pi} \sum_{n=-\infty}^{\infty} e^{jn(\phi - \phi')} \int_{-\infty}^{\infty} \frac{G_{lu}(n, k_z)}{2\pi d} P_e^u e^{-jk_z(z - z')} dk_z \tag{3.2}$$

where $G_{lu}(n, k_z)$ is the $\rho$-propagating series representation of the appropriate dyadic Green's function component which is explicitly given in [8] for both source and observation points located on the surface ($\rho = \rho' = d$). Both the Fourier summation and the Fourier integral in (3.2) converge very slowly for electrically large cylinders and large separations between the source and observation points. Therefore, large numbers for $n$ and $k_z$ are required to truncate these infinite

summation and integration to finite summation and integration, respectively. However, using large $n$ and $k_z$ values exhibit severe numerical problems due to the Hankel and Bessel functions (as well as their derivatives) which exist in the Green's function expression since both the order and argument of the functions depend on $n$ and $k_z$. To alleviate this problem, (3.2) is transformed to a more rapidly convergent $\phi$-propagating series representation using Watson's transform [8]. Provided that the cylinder is electrically large, retaining only the leading term, the surface field component is given by

$$E_l(z,\phi) \approx \frac{1}{2\pi}\int_{-\infty}^{\infty}\int_{-\infty-j\epsilon}^{\infty-j\epsilon} \frac{G_{lu}(\nu,k_z)}{2\pi d} P_e^u e^{-jk_z(z-z')} e^{j\nu(\phi-\phi')} d\nu \; dk_z \quad \epsilon > 0, \quad (3.3)$$

and then written in polar coordinates as

$$E_l(s,\delta) \approx \frac{1}{2\pi}\int_0^{\infty}\int_0^{2\pi} \frac{G_{lu}(\zeta,\psi)}{2\pi} P_e^u e^{j\zeta scos(\psi-\delta)} d\psi\zeta d\zeta \quad (3.4)$$

by performing the following transformations:

$$k_z = -\zeta cos\psi, \;\; \nu = \mu d, \;\; \mu = -\zeta sin\psi \quad (3.5)$$

and making use of the following geometrical substitutions:

$$r_l = d(\phi-\phi') = s \; sin\psi, \quad (z-z') = s \; cos\delta \quad (3.6)$$

where the definitions of $\psi$, $\delta$, $s$ and $\zeta$ are given in Fig. 3.2. An analysis of Green's function components $G_{lu}(\zeta,\psi)$ with respect to $\psi$ shows that $G_{lu}(\zeta,\psi)$ (all components) is periodic with $\pi$ (i.e. $G_{lu}(\zeta,\psi)$=$G_{lu}(\zeta,\psi+\pi)$). Therefore, it can be represented by a Fourier series as

$$G_{lu}(\zeta,\psi) \approx \sum_{n=0}^{N} a_n(\zeta) cos(2n\psi) + \sum_{n=1}^{N} b_n(\zeta) sin(2n\psi) \quad (3.7)$$

where $a_n(\zeta)$ and $b_n(\zeta)$ are Fourier series coefficients given by

$$a_n(\zeta) = \frac{\epsilon_n}{\pi}\int_T G_{lu}(\zeta,\psi) \; cos(2n\psi) \; d\psi \quad (3.8)$$

$$b_n(\zeta) = \frac{2}{\pi}\int_T G_{lu}(\zeta,\psi) \; sin(2n\psi) \; d\psi \quad (3.9)$$

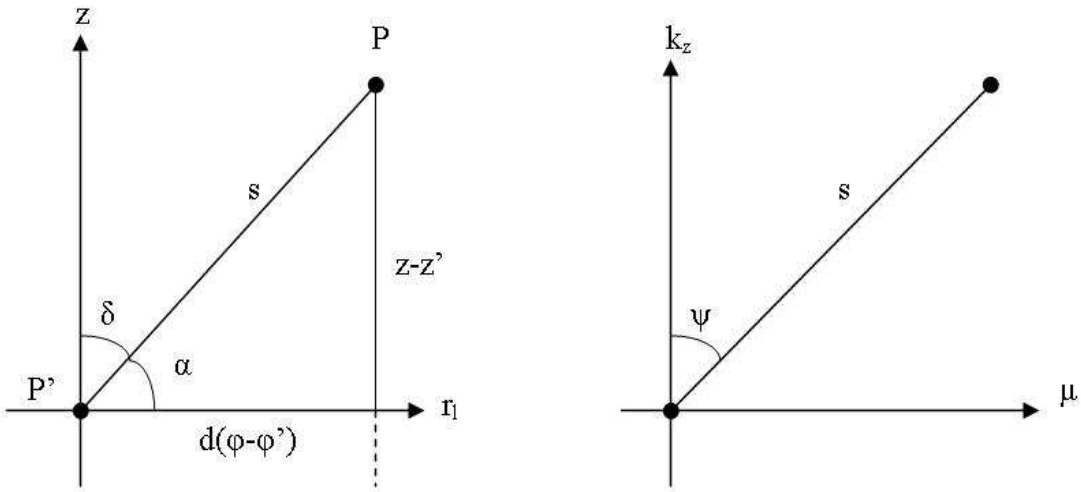


Figure 3.2: Space (s, $\delta$) and spectral ($\zeta$,$\psi$) polar coordinates.

with $\epsilon_n = 1$ for $n = 0$ and $\epsilon_n = 2$ for $n \neq 0$. These coefficients are functions of $\zeta$ only, which simplifies the surface field calculations significantly. The coefficients are calculated numerically by

$$a_n(\zeta) \approx \frac{\epsilon_n}{\pi} \sum_{p=1}^{P} w_p G_{lu}(\zeta, \psi_p)\ cos(2n\psi_p) \tag{3.10}$$

$$b_n(\zeta) \approx \frac{2}{\pi} \sum_{p=1}^{P} w_p G_{lu}(\zeta, \psi_p)\ sin(2n\psi_p) \tag{3.11}$$

where $w_p$ are the appropriate weights. Based on an investigation performed using the stationary phase method shows that the strongest contributions to the $\psi$-integral come from $\psi = \delta$ and $\psi = \pi + \delta$ ($\delta = 0$ axial direction) [17], [18]. Therefore, to obtain a valid solution within the paraxial region, the Green's function components $G_{lu}(\zeta, \psi)$ should be exact at least at $\psi = 0$. Based on this information, the abscissas $\psi_p$ in (3.11) should include $\psi = 0$ and $\psi = \pi$. Additionally making use of $\psi = 0,\ \pi/2$ and $\pi$ simplifies the numerical integration with respect to $\zeta$ in (3.4) due to the $sin(n\psi)$, $cos(n\psi)$ terms.

The essence of the method is the same for all components. However, each of them has unique features and hence, each has to be treated slightly different.

A) $\underline{G_{zz}(\zeta,\psi) \text{ component:}}$

In addition to its periodicity, $G_{zz}(\zeta,\psi)$ is even with respect to $\psi$ yielding $b_n = 0$. Only the leading two terms are retained to give the enough accuracy. Therefore, using a three-point trapezoidal rule [16] in the interval [0,$\pi$], the following expressions are found for $a_{0_{zz}}$ and $a_{1_{zz}}$

$$a_{0_{zz}}(\zeta) \approx \frac{1}{2}\left[G_{zz}(\zeta,\psi=0) + G_{zz}(\zeta,\psi=\frac{\pi}{2})\right] \tag{3.12}$$

$$a_{1_{zz}}(\zeta) \approx \frac{1}{2}\left[G_{zz}(\zeta,\psi=0) - G_{zz}(\zeta,\psi=\frac{\pi}{2})\right] \tag{3.13}$$

where the identity $G_{zz}(\zeta,\psi=0) = G_{zz}(\zeta,\psi=\pi)$ has been used to simplify the expressions. Substituting these expressions into (3.7), the expression for $G_{zz}(\zeta,\psi)$ is given by

$$\begin{aligned} G_{zz}(\zeta,\psi) \;\approx\; & G_{zz}(\zeta,\psi=\frac{\pi}{2}) + \Big[G_{zz}(\zeta,\psi=0) \\ & -G_{zz}(\zeta,\psi=\frac{\pi}{2})\Big]\left(\frac{1+cos\ 2\psi}{2}\right). \end{aligned} \tag{3.14}$$

B) $\underline{G_{\phi z}(\zeta,\psi)=G_{z\phi}(\zeta,\psi) \text{ component:}}$

$G_{\phi z}(\zeta,\psi)$, which is an odd function with respect to $\psi$ is given in [8] and can be written as

$$G_{\phi z}(\zeta,\psi) = \frac{\zeta^2 sin\ 2\psi}{2}\hat{G}_{\phi z}(\zeta,\psi). \tag{3.15}$$

In this expression, $\hat{G}_{\phi z}(\zeta,\psi)$ is an even function in $\psi$ and approximated with a FS where including only the leading term gives enough accuracy. The FS coefficient $a_{0_{\phi z}}(\zeta)$ is calculated by a numerical integration in the [0,$\pi$] interval using a two-point trapezoidal rule and is given by

$$a_{0_{\phi z}}(\zeta) \approx \frac{1}{\pi}\left[\frac{\pi}{2}(\hat{G}_{\phi z}(\zeta,\psi=0) + \hat{G}_{\phi z}(\zeta,\psi=\frac{\pi}{2}))\right] \;=\; \hat{G}_{\phi z}(\zeta,\psi=0) \tag{3.16}$$

yielding

$$G_{\phi z}(\zeta,\psi) \;\approx\; \frac{\zeta^2 sin\ 2\psi}{2}\hat{G}_{\phi z}(\zeta,\psi=0). \tag{3.17}$$

C) $G_{\phi\phi}(\zeta,\psi)$ component:

Following a similar procedure for the $G_{\phi\phi}$ component did not yield the same accuracy. Therefore, it is written as the sum of planar and curvature correction terms. Planar term corresponds to the limiting case of the cylindrical case when the outer and inner radii of the cylinder go to infinity while the thickness remains the same. On the other hand, curvature correction terms take the finite radius effects into account and as the radius of the cylinder decreases these terms become important. Consequently,

$$G_{\phi\phi}(\zeta,\psi) \approx G^{p}_{uu}(\zeta,\psi) + G^{cc}_{\phi\phi}(\zeta,\psi) \tag{3.18}$$

where $u = x$ or $y$, $p$ stands for "planar" and cc for "curvature correction". The planar term is already written in two-term FS expansion as:

$$G^{p}_{uu}(\zeta,\psi) = G^{p1}_{uu}(\zeta) - G^{p2}_{uu}(\zeta)\left(\frac{1-cos2\psi}{2}\right)\zeta^2 \tag{3.19}$$

and can be integrated in closed-form with respect to $\psi$. $G^{cc}_{\phi\phi}(\zeta,\psi)$ is even with respect to $\psi$ which implies that $b_n = 0$. Retaining only the first two terms of FS expansion gives accurate results. The following coefficients work well for $G^{cc}_{\phi\phi}(\zeta,\psi)$.

$$a_{0_{\phi\phi}}(\zeta) \approx \frac{1}{4}\left[G^{cc}_{\phi\phi}(\zeta,\psi=0) + G^{cc}_{\phi\phi}(\zeta,\psi=\frac{\pi}{2})\right] \tag{3.20}$$

$$a_{1_{\phi\phi}}(\zeta) \approx \frac{1}{4}\left[G^{cc}_{\phi\phi}(\zeta,\psi=0) - G^{cc}_{\phi\phi}(\zeta,\psi=\frac{\pi}{2})\right]. \tag{3.21}$$

Finally the $G_{\phi\phi}(\zeta,\psi)$ component is written as

$$\begin{aligned} G_{\phi\phi}(\zeta,\psi) \;\approx\; & G^{p1}_{uu}(\zeta) + \frac{1}{2}\,G^{cc}_{\phi\phi}(\zeta,\psi=0) - \zeta^2 G^{p2}_{uu}(\zeta)\left(\frac{1-cos2\psi}{2}\right) \\ & + \frac{1}{2}\left[G^{cc}_{\phi\phi}(\zeta,\psi=\frac{\pi}{2}) - G^{cc}_{\phi\phi}(\zeta,\psi=0)\right]\left(\frac{1-cos2\psi}{2}\right). \end{aligned} \tag{3.22}$$

These expressions for Green's function components (i.e. (3.14), (3.17) and (3.22)) are exact at $\psi = 0$, and they yield accurate results around paraxial region ($\delta \to 0$), but lose accuracy as $\delta$ becomes large for large values of $s$.

Surface field components are obtained by inserting these expressions for Green's function components into (3.4). Then $\psi$ integrals are calculated in closed-form using the relations given in (3.23)-(3.26), namely

$$\int_0^{2\pi} \frac{e^{j\zeta s\ cos(\psi-\delta)}}{2\pi}\, d\psi \;=\; J_0(\zeta s) \tag{3.23}$$

$$\int_0^{2\pi} \left(\frac{1-cos\ 2\psi}{4\pi}\right) e^{j\zeta s\ cos(\psi-\delta)}\, d\psi \;=\; -\frac{1}{\zeta^2}\frac{\partial^2}{\partial r_l^2} J_0(\zeta s) \tag{3.24}$$

$$\int_0^{2\pi} \left(\frac{1+cos\ 2\psi}{4\pi}\right) e^{j\zeta s\ cos(\psi-\delta)}\, d\psi \;=\; -\frac{1}{\zeta^2}\frac{\partial^2}{\partial z^2} J_0(\zeta s) \tag{3.25}$$

$$\int_0^{2\pi} \frac{sin\ 2\psi}{4\pi} e^{j\zeta s\ cos(\psi-\delta)}\, d\psi \;=\; -\frac{1}{\zeta^2}\frac{\partial^2}{\partial r_l \partial z} J_0(\zeta s). \tag{3.26}$$

The final expressions for surface fields are given by (3.27), (3.28), (3.29).

$$E_{zz}(\delta,s) \;\approx\; \frac{-Z_0 p_e^z}{2\pi k_0} \left\{ k_0^2 P(s) + \frac{\partial^2}{\partial z^2}\left[P(s)-Q(s)\right]\right\} \tag{3.27}$$

$$E_{\phi z}(\delta,s) \;\approx\; \frac{-Z_0 p_e^z}{2\pi k_0}\frac{\partial^2}{\partial z \partial r_l}\left\{M(s)-R(s)\right\} \tag{3.28}$$

$$E_{\phi\phi}(\delta,s) \;\approx\; \frac{-Z_0 p_e^\phi}{2\pi k_0} \left\{ k_0^2 U(s) + \frac{\partial^2}{\partial r_l^2}\left[U(s) - \frac{\epsilon_r - 1}{\epsilon_r} W(s)\right]\right\} + \frac{jZ_0 p_e^\phi}{4\pi k_0}\left\{ S(s) - \frac{\partial^2}{\partial r_l^2} T(s)\right\} \tag{3.29}$$

where P(s), Q(s), M(s), R(s), W(s), U(s), S(s) and T(s) are special functions which are explicitly given in [18] and [17]. Note that $U(s)$ and $W(s)$ are the same

special functions used for the Sommerfeld integral representation for the planar single layer microstrip dyadic Green's function as given in (2.11), (2.12) and [20].

The integrals of these special functions are evaluated numerically along the real axis using a Gaussian quadrature algorithm, where an envelope extraction technique is used in all to overcome the difficulties in the numerical integration arising from their integrands' oscillatory as well as slowly decaying behaviours. Furthermore, the singularities which are on the real axis (for lossless case) along the path of integration are handled by regularizing the integrands. More details about the numerical integrations can be found in [8].

This method is approximately five times faster than the eigenfunction solution. Moreover, the calculation time by this method is fairly independent of the cylinder's radius (for radii $\geq \lambda_0$), whereas, for the eigenfunction solution, it increases as the electrical size of the cylinder becomes greater. This shows that this method is much more efficient than eigenfunction solution for electrically large cylinders.

# Chapter 4

# Development of an Asymptotic Closed-Form Expression for Green's Function of Dielectric Coated PEC Cylinder

## 4.1 Introduction

In this chapter, the development of the asymptotic closed-form expressions for the Green's function of dielectric coated circular PEC cylinder is presented in detail, which is the main contribution of this thesis. The starting point of the development process is the final results of [18]. Then, a procedure similar to the procedure given in [20] is applied to reach the final asymptotic closed-form expressions.

## 4.2 Formulation

The development of the formulation follows the results of [18] which is explained in chapter 3 and given in (3.27)-(3.29).

In these expressions P(s), Q(s), M(s), R(s), W(s), U(s), S(s) and T(s) are special functions which are explicitly given in [17], [18]. Once these functions are calculated, electric field components can be found easily. All of these special functions are in the Sommerfeld integration form and can not be evaluated exactly. During the numerical integration, their rate of convergence is nearly identical. Their integrands possess a Bessel function of the first kind ($J_0(\zeta s)$) and they are odd functions of the integration variable $\zeta$. Therefore, the same procedure is implemented for all of them.

Consider the following Y function which have the same generic form as the special functions mentioned above.

$$Y = \int_0^\infty G^{cyl}(\xi)\, e^{-j\sqrt{k_0^2-\xi^2}\,\rho}\, J_0(s\xi)\, d\xi \tag{4.1}$$

where $\rho$ is the radial distance from the air-dielectric interface ($\rho = 0$) and is small. Since the integrand $G^{cyl}$ is an odd function of the integration variable $\xi$, it can be transformed into the Hankel form given by

$$Y = \frac{1}{2}\int_{-\infty}^\infty G^{cyl}(\xi)\, e^{-j\sqrt{k_0^2-\xi^2}\,\rho}\, H_0^{(2)}(s\xi)\, d\xi. \tag{4.2}$$

The integration contour for (4.2) is shown in Fig. 2.2 by Sommerfeld contour label. Next, similar to the planar case, the integration contour is deformed around the branch-cut as shown in Fig. 2.2. The integrand of (4.2) may have poles in the lower half $\xi$-plane. The imaginary parts of these poles are negative so they are the proper surface-wave poles. During the deformation these poles must be captured. The integration around the branch-cut can be transformed to a real axis integration by the change of variables given by (2.18). The result of this

transformation is the expression given by

$$Y = \int_{-\infty}^{\infty} F^{cyl}(\zeta)\, e^{-j\zeta\rho}\, H_0^{(2)}\left(s\sqrt{k_0^2-\zeta^2}\right)\, d\zeta$$

$$-2\pi j \sum_n Res_Y(\zeta_n). \tag{4.3}$$

Note that, the new integrand in (4.3) is denoted by $F^{cyl}$ since the change of variables and transformations alter the integrand. Now consider the integration term of (4.3):

$$I = \int_{-\infty}^{\infty} F^{cyl}(\zeta)\, e^{-j\zeta\rho}\, H_0^{(2)}\left(s\sqrt{k_0^2-\zeta^2}\right)\, d\zeta \tag{4.4}$$

which is in the same form of (2.22) but the integrand is for the electrically large coated circular cylinder. In general the $F^{cyl}$ function in the integrand may have surface or/and leaky wave poles at $\zeta_p^{cyl}$ close to $\zeta = 0$. So it may be written in a series form given by

$$F^{cyl}(\zeta) = \sum_n a_n \zeta^n + \sum_p \frac{R_{F^{cyl}}(\zeta_p^{cyl})}{\zeta - \zeta_p^{cyl}} \tag{4.5}$$

where $R_{F^{cyl}}(\zeta_p^{cyl})$ is the residue of $F^{cyl}(\zeta)$ at $\zeta = \zeta_p^{cyl}$ and $a_n$ are the coefficients of the power series. Substituting (4.5) into (4.4) and performing the same change of variables given by (2.24) the integral denoted by $I$ can be obtained as

$$I = k_0 \sum_n \frac{a_n}{(-j)^n} \frac{\partial}{\partial \rho^n} \int_{-\infty}^{\infty} H_0^{(2)}\left(k_0 s\sqrt{1-\eta^2}\right) e^{-jk_0\eta\rho} d\eta$$

$$+ \sum_p R_{F^{cyl}}(\zeta_p^{cyl}) \int_{-\infty}^{\infty} \frac{H_0^{(2)}\left(k_0 s\sqrt{1-\eta^2}\right)}{\eta - \eta_p^{cyl}} e^{-jk_0\eta\rho} d\eta, \tag{4.6}$$

which is very similar to (2.25) for the planar case. The first term of (4.6) can be calculated in closed-form by noting that

$$I_0 = \int_{-\infty}^{\infty} H_0^{(2)}(k_0 s\sqrt{1-\eta^2}) e^{-jk_0\eta\rho} d\eta$$

$$= 2j \frac{e^{-jk_0\sqrt{s^2+\rho^2}}}{k_0\sqrt{s^2+\rho^2}}, \tag{4.7}$$

and

$$I_n = \frac{k_0^n}{(-j)^n}\frac{\partial}{\partial\rho^n}\int_{-\infty}^{\infty} H_0^{(2)}\left(k_0 s\sqrt{1-\eta^2}\right) e^{-jk_0\eta\rho}d\eta,$$
$$= \frac{k_0^n}{(-j)^n}\ \frac{\partial}{\partial\rho^n}\ \left(2j\frac{e^{-j\sqrt{k_0^2+\rho^2}}}{\sqrt{k_0^2+\rho^2}}\right). \tag{4.8}$$

$I_{n=even}$ is calculated in closed-form via (4.8), but $I_{n=odd}=0$. For the second term of (4.6) the large-argument approximation for the Hankel function given by (2.28) is applied. So, the second integral of (4.6) is approximated as

$$I_s \approx \sqrt{\frac{2}{\pi k_0 s}}e^{j\pi/4}\int_{-\infty}^{\infty}\frac{1}{(\sqrt{1-\eta^2})^{1/2}}\left(1+\frac{j}{8k_0 s\sqrt{1-\eta^2}}\right)$$
$$\cdot\frac{e^{-jk_0(s\sqrt{1-\eta^2}+\eta\rho)}}{\eta-\eta_p^{cyl}}d\eta \tag{4.9}$$

which has the same form as that of (2.27). The definitions of the branch-cuts are similar to the planar case. Namely, because of $\sqrt{1-\eta^2}$ terms in the integrand, $\eta$-plane is a two-sheeted complex plane with two branch points at $\eta=\pm1$. The branch-cuts extend to infinity and determined such that $Im(\sqrt{1-\eta^2})<0$ on the entire top sheet. The integration in (4.9) is performed along the real axis on the top sheet. However, we can map this two-sheeted $\eta$-plane to a single plane by the same angular spectrum mapping given by (2.29). Then performing the following polar transform

$$s = r\ sin\ \theta\ \ ;\ \ \rho = r\ cos\ \theta \tag{4.10}$$

(4.9) becomes

$$I_s \approx \sqrt{\frac{2}{\pi k_0 r\ sin\ \theta}}e^{j\pi/4}\int_{\Gamma}\left(1+\frac{j}{8k_0 r\ sin\ \theta\ sin\ \gamma}\right)\frac{1}{\sqrt{sin\ \gamma}}$$
$$\cdot\frac{e^{-jk_0 r\ cos\ (\theta-\gamma)}}{cos\ \gamma-cos\ \gamma_p^{cyl}}\ sin\ \gamma\ d\gamma. \tag{4.11}$$

By this way different quarters of two sheets of $\eta$-plane are mapped into different adjacent sections of width $\frac{\pi}{2}$ in the complex $\gamma$ plane ($-\pi/2 \le Re\ \gamma \le 3\pi/2$).

The integral in (4.11) has a saddle point at $\gamma_s=0$. The contour $\Gamma$ in (4.11) can be deformed into the steepest descent path (SDP) through the saddle point

in the complex $\gamma$ plane. This integration contour can be transformed to a real axis integration by the following change of variables:

$$-j(cos\ (\theta-\gamma)-1) = -x^2\ \ ;\ \ d\gamma\ =\ \frac{2j}{\sqrt{x^2+2j}}dx. \tag{4.12}$$

After this deformation of the integration path, the integral in (4.11) can be written as (similar to the planar case)

$$\begin{aligned} I_s\ \ &\approx\ \ 2\pi jN(\eta_p^{cyl})H_0^{(2)}(k_0s\sqrt{1-(\eta_p^{cyl})^2}\ )e^{-jk_0\eta_p\rho} \\ &\quad +\sqrt{\frac{2}{\pi\ k_0\ s}}e^{j\pi/4}e^{-jk_0r}\int_{-\infty}^{\infty}G(x)e^{-k_0rx^2}dx \end{aligned} \tag{4.13}$$

where

$$G(x)\ =\ \left(1+\frac{j}{8k_0s\ sin\ \gamma}\right)\ \frac{\sqrt{sin\ \gamma}}{cos\ \gamma\ -\ cos\ \gamma_p^{cyl}}\ \frac{d\gamma}{dx}. \tag{4.14}$$

In this expression, the first term accounts for the residues of poles captured during the deformation of integration path into the steepest descent path. Here $N(\eta_p)$ is given by (2.34). The second term is the integration term along the SDP.

An approximate closed-form solution for (4.13) can now be written for $k_0r \gg 1$ by taking the leading term of uniform asymptotic expression for the integration term [22]. The closed-form expression is obtained as

$$\begin{aligned} I_s \approx M(k_0r,\eta_p^{cyl})\ \ &=\ \ 2\pi jN(\eta_p^{cyl})H_0^{(2)}(k_0s\ sin\ \gamma_p^{cyl})e^{-jk_0\rho\ cos\ \gamma_p^{cyl}} \\ &\quad +2j\ \frac{e^{-jk_0r}}{k_0r}\ \left(1+\frac{j}{8k_0r\ sin^2\theta}\right) \\ &\quad \left[\frac{1}{cos\ \theta-cos\ \gamma_p^{cyl}}-\frac{1}{2\sqrt{sin\theta}\sqrt{sin\ \gamma_p^{cyl}}\ sin\ \left(\frac{\gamma_p^{cyl}-\theta}{2}\right)}\right. \\ &\quad \left.\left(1-F\left(2k_0\ r\ sin^2\left(\frac{\gamma_p^{cyl}-\theta}{2}\right)\right)\right)\right] \end{aligned} \tag{4.15}$$

where positive branch of $\sqrt{sin\ \gamma_p^{cyl}}$ is used and $F(x)$ is the transition function given by (2.36).

There are two special conditions for the cases investigated in this thesis. Firstly, source and observation points are both at the dielectric-air interface. That is $\rho = 0$ and $\theta = \frac{\pi}{2}$. Secondly, the dielectric is assumed to be lossless. At these special conditions, the integral I given by (4.4) can be approximated as

$$I \approx k_0 a_0 I_0 + k_0^3 a_2 I_2 + \sum_p R_{F^{cyl}}(\zeta_p^{cyl}) M(k_0 s, \eta_p^{cyl}) \tag{4.16}$$

where

$$I_0 = \int_{-\infty}^{\infty} H_0^{(2)}(k_0 s\sqrt{1-\eta^2}) e^{-jk_0\eta\rho} d\eta \Big|_{\rho=0} = 2j\frac{e^{-jk_0 s}}{k_0 s} \tag{4.17}$$

$$I_{n=odd} = 0 \quad (\Rightarrow \quad I_1 = 0) \tag{4.18}$$

$$I_2 = \int_{-\infty}^{\infty} H_0^{(2)}(k_0 s\sqrt{1-\eta^2}) e^{-jk_0\eta\rho}\eta^2 \, d\eta \Big|_{\rho=0} = \frac{-2e^{-jk_0 s}}{(k_0 s)^2}\left(1 + \frac{1}{jk_0 s}\right) \tag{4.19}$$

and $M(k_0 s, \eta_p)$ is given by

$$M(k_0 s, \eta_p^{cyl}) = -2\pi j N(\eta_p^{cyl}) H_0^{(2)}(k_0 s\sqrt{1-(\eta_p^{cyl})^2}) \tag{4.20}$$

$$-2j \; \frac{e^{-jk_0 s}}{k_0 s \eta_p^{cyl}} \; \left(1 + \frac{j}{8k_0 s}\right)$$

$$\left[1 + \frac{\eta_p^{cyl}}{2\sqrt{sin\gamma_p^{cyl}} \; sin(\frac{\gamma_p^{cyl}}{2} - \frac{\pi}{4})} \left(1 - F\left(2k_0 \; s \; sin^2(\frac{\gamma_p^{cyl}}{2} - \frac{\pi}{4})\right)\right)\right]$$

and $N(\eta_p^{cyl}) = 0$ since no surface wave pole is captured during deformation of integration path to SDP if $\rho = 0$.

For the lossless case all the cylindrical poles will be on the imaginary axis and show the same characteristics as the planar case, namely:

$$\eta_p^{cyl} = \pm j|\eta_p^{cyl}| \begin{cases} (-) & \text{for proper surface wave} \\ (+) & \text{for improper surface wave} \end{cases} \tag{4.21}$$

and

$$\gamma_p^{cyl} = cos^{-1}(\eta_p^{cyl}) = \frac{\pi}{2} \pm j(\gamma_p^{cyl})'' \begin{cases} (+) & \text{for proper surface wave} \\ (-) & \text{for improper surface wave.} \end{cases} \tag{4.22}$$

Therefore,

$$sin\left(\frac{\gamma_p^{cyl}}{2}-\frac{\pi}{4}\right) = \pm\frac{j}{\sqrt{2}}\sqrt{\sqrt{1+|\eta_p^{cyl}|^2}-1}\begin{cases}(+) & \text{for proper surface wave}\\ (-) & \text{for improper surface wave.}\end{cases} \tag{4.23}$$

Finally, $a_n$ terms are calculated by Taylor expansion of integrand of (4.4) excluding the Hankel function and the residue term of (4.5). The Taylor expansion of the residue term of (4.5) is given as follows:

$$\frac{R_{F^{cyl}}(\zeta_p^{cyl})}{\zeta-\zeta_p^{cyl}} = -\frac{R_{F^{cyl}}(\zeta_p^{cyl})}{\zeta_p^{cyl}}\left(1+\frac{\zeta}{\zeta_p^{cyl}}+\frac{\zeta^2}{(\zeta_p^{cyl})^2}+...\right). \tag{4.24}$$

At the end of all these steps, all special functions involved in (3.27)-(3.29) are written in a special form given by

$$\begin{aligned} Y &= \left[f_{a0_Y}(d)+\sum_{p_Y}\left(\frac{R_Y(\zeta_{p_Y}^{cyl})}{\zeta_{p_Y}^{cyl}}\right)\right]k_0I_0 \;+\\ &\quad\left[f_{a2_Y}(d)+\sum_{p_Y}\left(\frac{R_Y(\zeta_{p_Y}^{cyl})}{(\zeta_{p_Y}^{cyl})^3}\right)\right]k_0I_2 \;+\\ &\quad\sum_{p_Y}R_Y(\zeta_{p_Y})M(k_0s,\eta_{p_Y}^{cyl})-2\pi j\sum_n Res_Y(\zeta_n^{cyl}), \end{aligned} \tag{4.25}$$

though the corresponding $f_{a0_Y}(d)$ and $f_{a2_Y}(d)$ functions, poles and corresponding residues will vary among them. These equations have a similar mathematical form as the equations for planar microstrip structures. Furthermore, they reduce to their planar counterparts when the radius of the cylinder (both inner and outer radii) goes to infinity while the thickness remains the same. The main differences come from $f_{a0_Y}(d)$ and $f_{a2_Y}(d)$ functions and the values of poles and corresponding residues of the cylindrical special functions. The calculation procedure for $f_{a0_Y}(d)$ and $f_{a2_Y}(d)$ are similar to the planar case but show some major differences since they are outer radius dependent parameters. Furthermore, accuracy of (4.25) strongly depends on the correct derivation of $f_{a0_Y}(d)$ and $f_{a2_Y}(d)$. In the planar case [20] when the power series expansion around $\zeta=0$ is performed, only $a_2$ is found explicitly, since $a_0=0$ and because $I_1=0$, $a_1$ is not necessary. This is the same in $Y=U$ and $W$ in our case, since they correspond to the planar terms. However, for the other special functions, a direct power series expansion of $\tilde{F}_p(\zeta)$

which is given by

$$\tilde{F}_p = F^{cyl} - \sum_p \frac{R_{F^{cyl}}(\zeta_p^{cyl})}{\zeta - \zeta_p^{cyl}} \tag{4.26}$$

around $\zeta = 0$ yields radius-dependent coefficients which diverge when the radius of the cylinder goes to infinity. Therefore, first an asymptotic expansion of $\tilde{F}_p(\zeta)$ is performed with respect to $1/d$ as

$$\tilde{F}_p(\zeta) = \tilde{F}_0(\zeta) + \frac{\tilde{F}_1(\zeta)}{d} + \frac{\tilde{F}_2(\zeta)}{d^2} + ... \tag{4.27}$$

where only the three terms ($\tilde{F}_0(\zeta)$, $\tilde{F}_1(\zeta)$ and $\tilde{F}_2(\zeta)$) are included. Then, a power series expansion around $\zeta = 0$ is performed for each $\tilde{F}_i$ $(i = 1,\ 2,\ 3)$ such that

$$\tilde{F}_i(\zeta) = a_{0\,i} + a_{1\,i}\zeta + a_{2\,i}\zeta^2 + ... \tag{4.28}$$

Finally, $f_{a0_Y}(d)$ and $f_{a2_Y}(d)$ functions are obtained as follows:

$$f_{a0_I}(d) = a_{0\,0} + \frac{a_{0\,1}}{d} + \frac{a_{0\,2}}{d^2} \tag{4.29}$$

$$f_{a2_I}(d) = a_{2\,0} + \frac{a_{2\,1}}{d} + \frac{a_{2\,2}}{d^2}. \tag{4.30}$$

$f_{a0_Y}(d)$ and $f_{a2_Y}(d)$ expressions for all special functions are explicitly given in Appendix B. Explicit expressions for residues of individual functions are given in Appendix C.

By this formulation, all the special functions denoted by $Y$ and thus the surface fields (Green's function) along the paraxial region of an electrically large dielectric coated circular cylinder is asymptotically evaluated in closed-form for relatively large separations. Note that this asymptotic formulation reduces to the asymptotic formulation of the planar case given by (2.44) and (2.46) when the radius of the cylinder goes to infinity (but the thickness remains the same.)

# Chapter 5

# Numerical Results

In this section a few numerical results are given to show the accuracy of the asymptotic approach compared to the standard eigenfunction solution and FS solution. To test the accuracy, mutual impedance between two tangential current components are calculated. In numerical calculations, the parameters of cylinder are; inner radius $a = 3\lambda_0$, dielectric thickness $t_h = 0.06\lambda_0$, $\epsilon_r = 3.25$ ($\lambda_0 =$ free-space wavelength). Note that the mutual impedance $Z_{nm}$ between the two current modes is simply given by

$$Z_{nm} = \int_{S_m} \mathbf{E}_n \cdot \mathbf{J}_m \, ds \tag{5.1}$$

where $\mathbf{E}_n$ is the field due to source (current mode) $\mathbf{J}_n$ and $S_m$ is the area occupied by source (current mode) $\mathbf{J}_m$. The current modes are defined by a piecewise sinusoid along the direction of the current and by a constant along the direction perpendicular to the current. The definition for piecewise sinusoid is given in (2.55). Each element has dimensions of $0.05\lambda_0$ (along the direction of the current) by $0.02\lambda_0$. This particular choice of current modes alleviates the convergence of the reference eigenfunction solution for large cylinders.

In Figures 5.1 and 5.2, the real and imaginary parts of $Z_{12}$ (mutual coupling) between two $\hat{z}$-directed current modes are plotted versus separation, by the three methods. Source and observation points lie on the $\hat{z}$-axis ($\alpha = 90°$). In Figures 5.3 and 5.4, $\alpha$ is changed to 70° for the same calculation, so that we have a deviation

from the axial region. In Figures 5.5 and 5.6, the real and imaginary parts of $Z_{12}$ (mutual coupling) between one $\hat{z}$-directed and one $\hat{\phi}$-directed current modes are plotted versus separation, by the three methods. Source and observation points lie nearly on the $\hat{z}$-axis where $\alpha$ is set to 88° since for $\alpha = 90°$ the mutual coupling is exactly zero. In Figures 5.7 and 5.8, $\alpha$ is changed to 70° for the same coupling case. In Figures 5.9 and 5.10, the real and imaginary parts of $Z_{12}$ (mutual coupling) between two $\hat{\phi}$-directed current modes are plotted versus separation, again by using these three methods. Source and observation points lie on the $\hat{z}$-axis ($\alpha = 90°$). Finally, in Figures 5.11 and 5.12, $\alpha$ is changed to 70° for the same $\hat{\phi} - \hat{\phi}$ coupling. For these parameters (dielectric constant $\epsilon_r$, dielectric thickness ($t_h$), and radius of cylinder) asymptotic solution involves two poles namely, one TM surface wave pole and one TE leaky wave pole.

The figures show that, the developed asymptotic closed-form solution yields very accurate results for separations greater than 0.8-0.9$\lambda_0$ along the paraxial region. Accuracy increases as the separation as well as the radius of the cylinder increase. The convergence problems associated with the eigenfunction solution as the separation gets larger are apparent from the plots. As the separation increases (over 6-7$\lambda_0$ for $\hat{z} - \hat{\phi}$ case and over 5$\lambda_0$ for $\hat{\phi} - \hat{\phi}$ case), the eigenfunction solution completely fails while FS and asymptotic solution do not have such a problem. Also due to the Sommerfeld integration form FS solution is expected to fail after $10 - 12\lambda_0$ separations. On the other hand in terms of their efficiency, the following table illustrates the CPU times spent to generate the data needed for the Figures 5.1 to 5.12.

| Case | Time(seconds) | |
|---|---|---|
| | Asymptotic Closed-Form | Fourier Series |
| $\hat{z} - \hat{z}$ (90°) | 0.44 | 198 |
| $\hat{z} - \hat{z}$ (70°) | 0.41 | 193.5 |
| $\hat{z} - \hat{\phi}$ (88°) | 0.11 | 15.2 |
| $\hat{z} - \hat{\phi}$ (70°) | 0.11 | 15.3 |
| $\hat{\phi} - \hat{\phi}$ (90°) | 0.49 | 141.5 |
| $\hat{\phi} - \hat{\phi}$ (70°) | 0.49 | 141.65 |

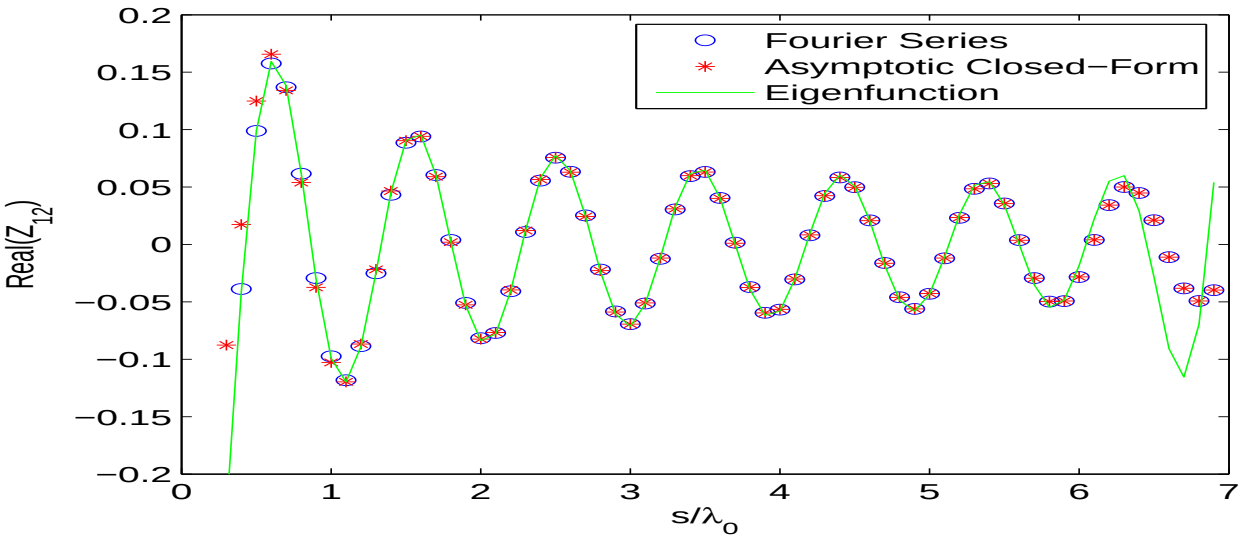


Figure 5.1: Real part of the mutual impedance ($Z_{12}$) between two identical $\hat{z}-$directed current sources versus separation $s$ when $\alpha = 90°$ for a coated cylinder with $a = 3\lambda_0$, $t_h = 0.06\lambda_0$, $\epsilon_r = 3.25$.

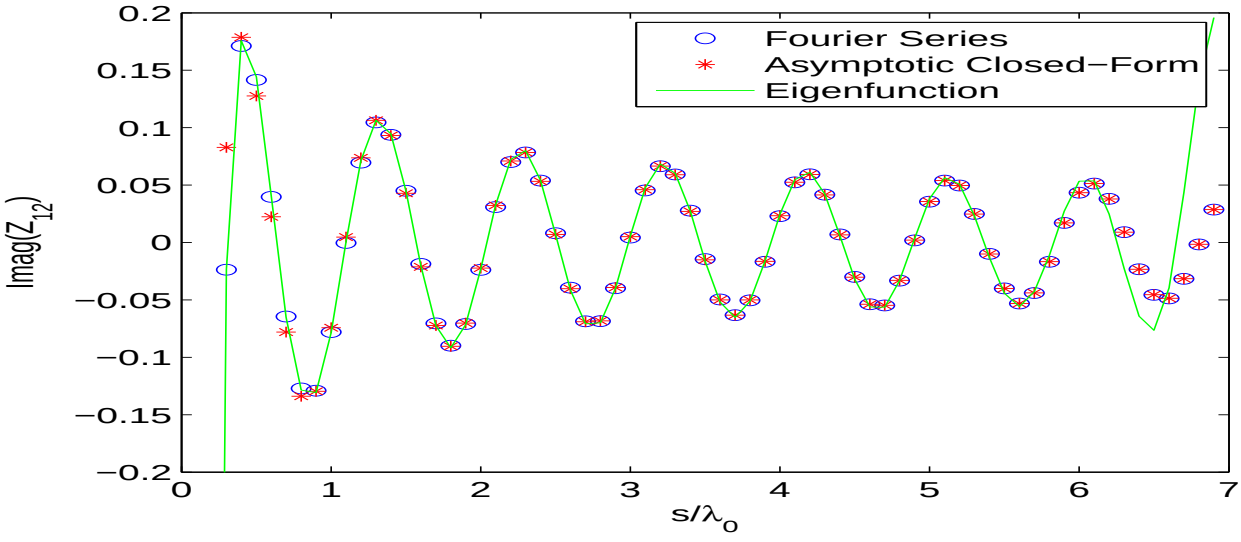


Figure 5.2: Imaginary part of the mutual impedance ($Z_{12}$) between two identical $\hat{z}-$directed current sources versus separation $s$ when $\alpha = 90°$ for a coated cylinder with $a = 3\lambda_0$, $t_h = 0.06\lambda_0$, $\epsilon_r = 3.25$.

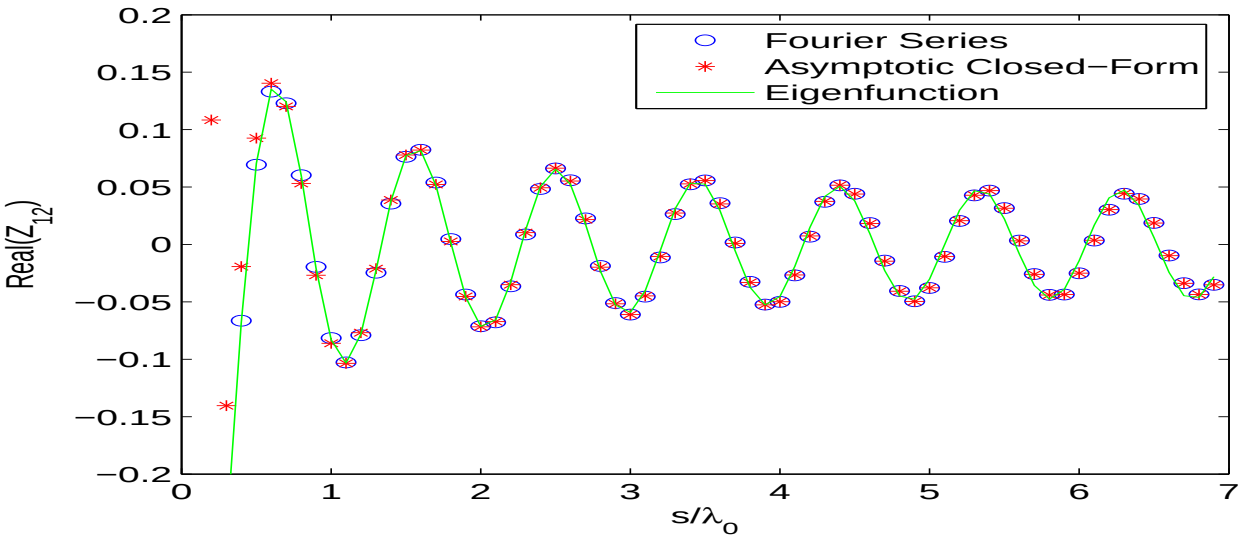


Figure 5.3: Real part of the mutual impedance ($Z_{12}$) between two identical $\hat{z}-$directed current sources versus separation $s$ when $\alpha = 70°$ for a coated cylinder with $a = 3\lambda_0$, $t_h = 0.06\lambda_0$, $\epsilon_r = 3.25$.

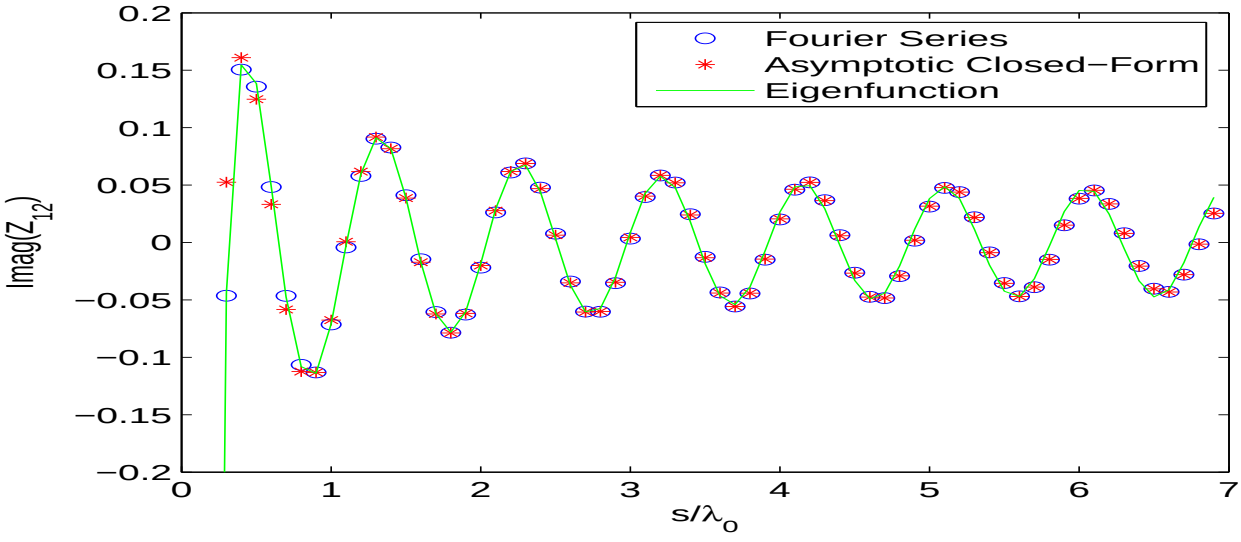


Figure 5.4: Imaginary part of the mutual impedance ($Z_{12}$) between two identical $\hat{z}-$directed current sources versus separation $s$ when $\alpha = 70°$ for a coated cylinder with $a = 3\lambda_0$, $t_h = 0.06\lambda_0$, $\epsilon_r = 3.25$.

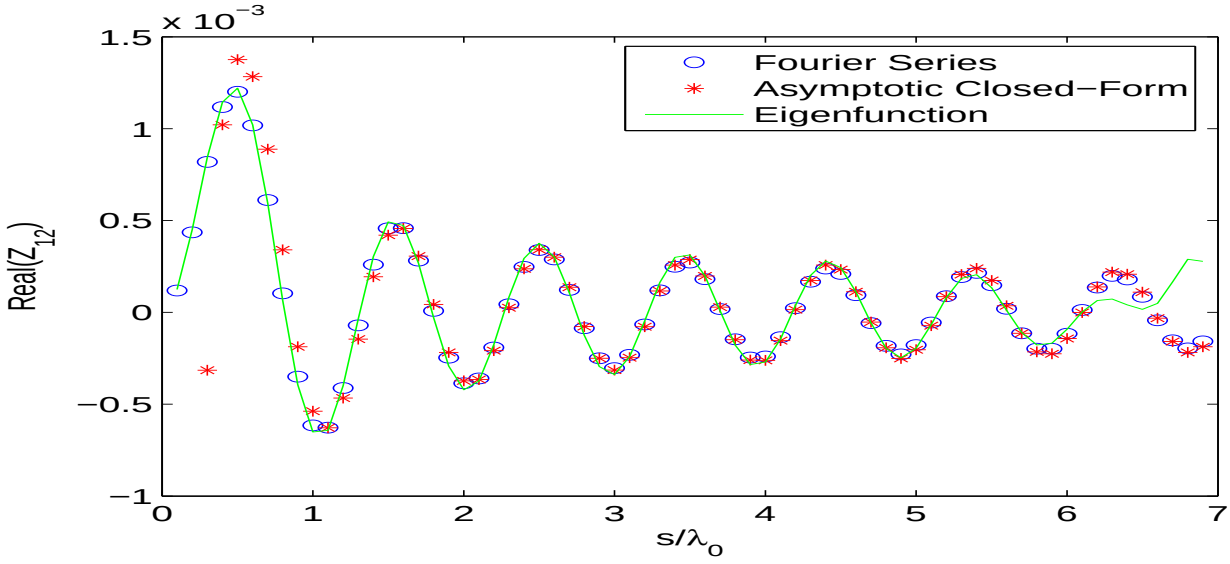


Figure 5.5: Real part of the mutual impedance ($Z_{12}$) between one $\hat{z}-$directed and one $\hat{\phi}-$directed current sources versus separation $s$ when $\alpha = 88°$ for a coated cylinder with $a = 3\lambda_0$, $t_h = 0.06\lambda_0$, $\epsilon_r = 3.25$.

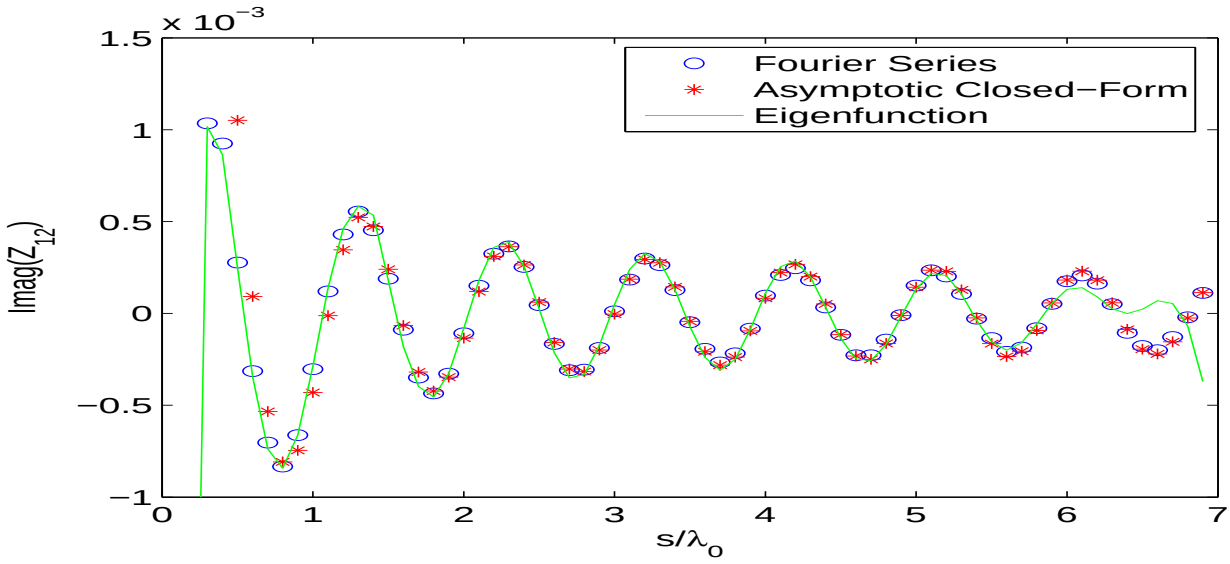


Figure 5.6: Imaginary part of the mutual impedance ($Z_{12}$) between one $\hat{z}-$directed and one $\hat{\phi}-$directed current sources versus separation $s$ when $\alpha = 88°$ for a coated cylinder with $a = 3\lambda_0$, $t_h = 0.06\lambda_0$, $\epsilon_r = 3.25$.

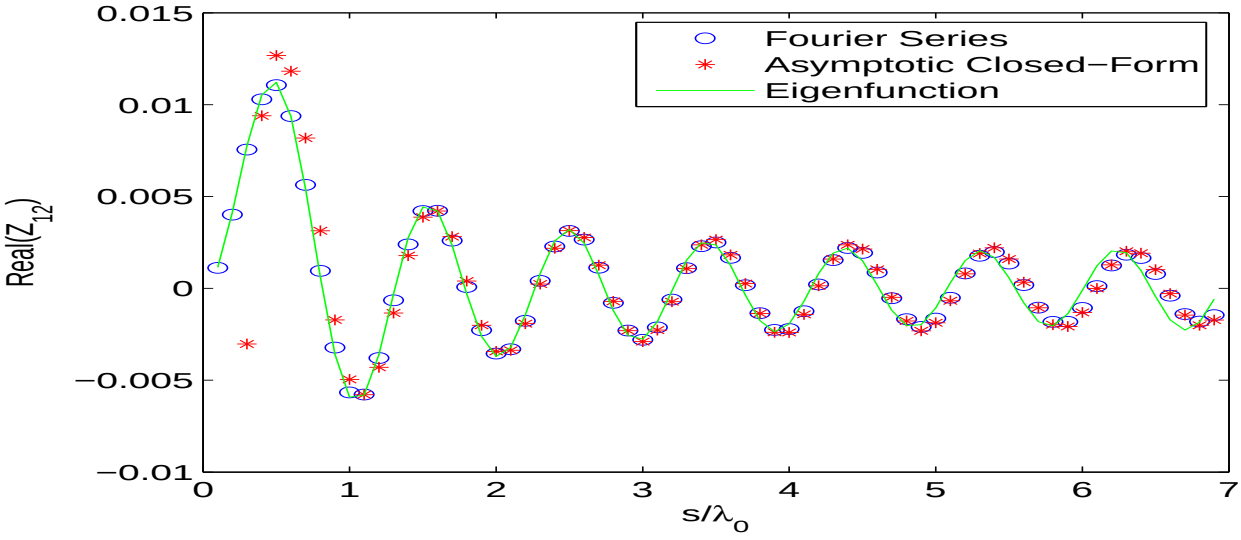


Figure 5.7: Real part of the mutual impedance ($Z_{12}$) between one $\hat{z}-$directed and one $\hat{\phi}-$directed current sources versus separation $s$ when $\alpha = 70°$ for a coated cylinder with $a = 3\lambda_0$, $t_h = 0.06\lambda_0$, $\epsilon_r = 3.25$.

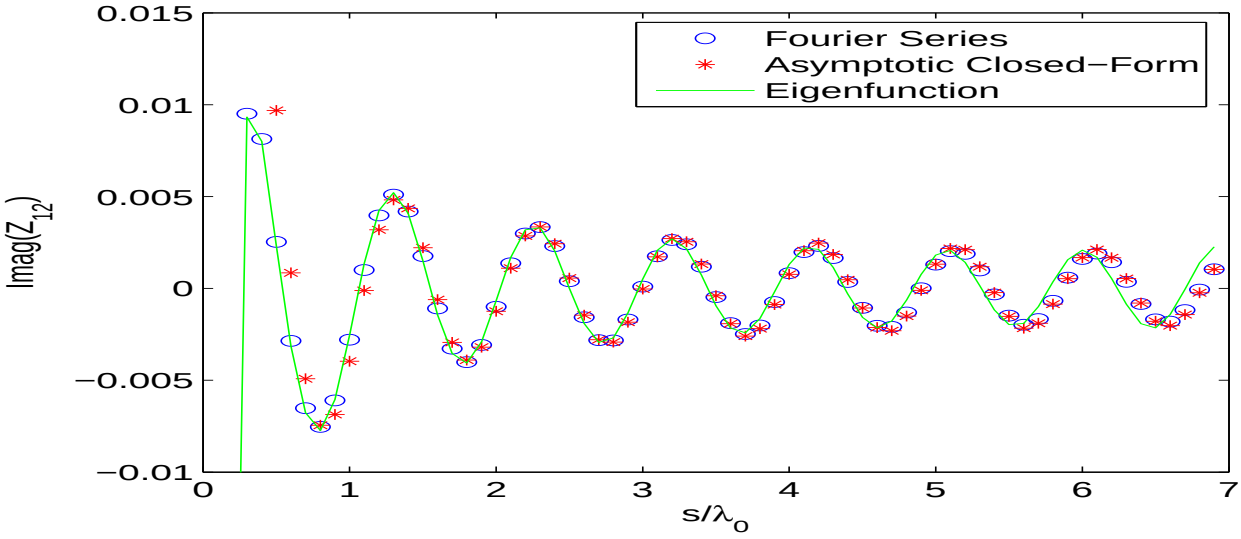


Figure 5.8: Imaginary part of the mutual impedance ($Z_{12}$) between one $\hat{z}-$directed and one $\hat{\phi}-$directed current sources versus separation $s$ when $\alpha = 70°$ for a coated cylinder with $a = 3\lambda_0$, $t_h = 0.06\lambda_0$, $\epsilon_r = 3.25$.

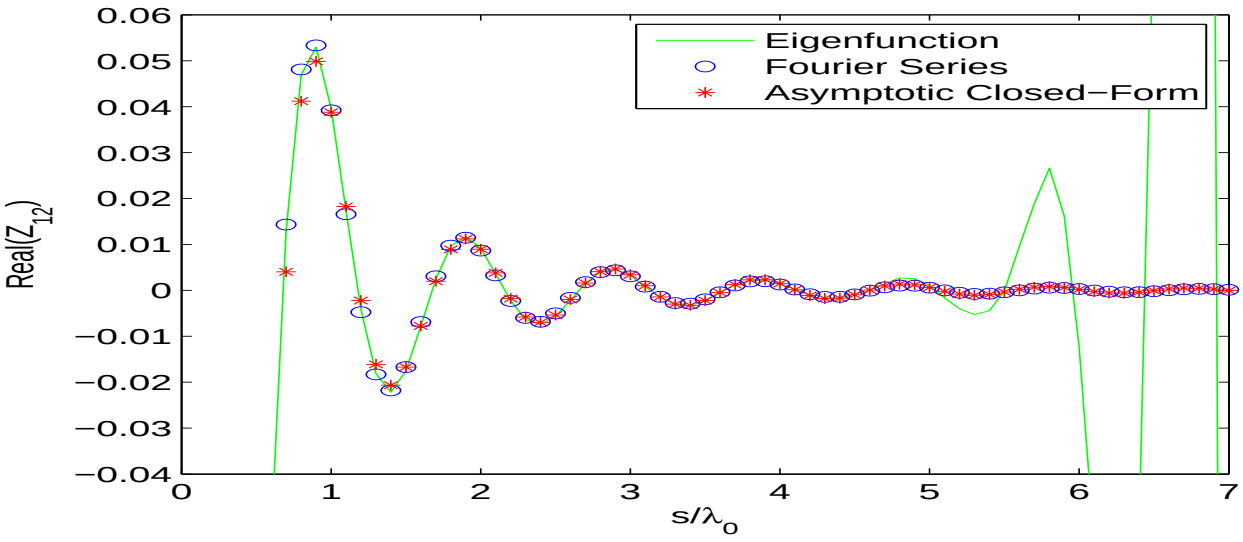


Figure 5.9: Real part of the mutual impedance ($Z_{12}$) between two identical $\hat{\phi}-$directed current sources versus separation $s$ when $\alpha = 90°$ for a coated cylinder with $a = 3\lambda_0$, $t_h = 0.06\lambda_0$, $\epsilon_r = 3.25$.

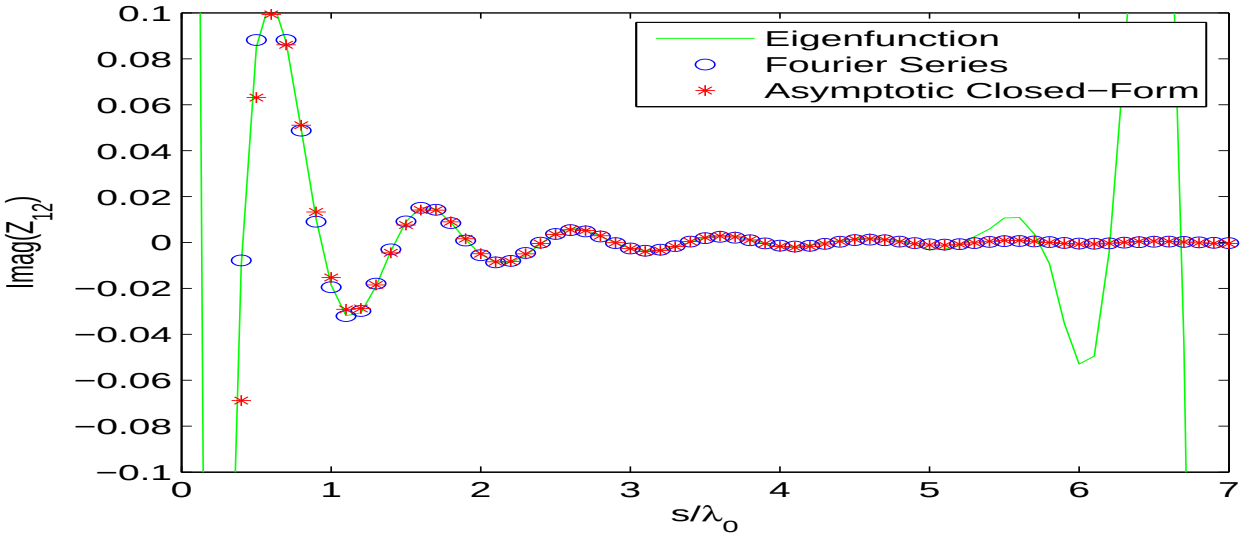


Figure 5.10: Imaginary part of the mutual impedance ($Z_{12}$) between two identical $\hat{\phi}-$directed current sources versus separation $s$ when $\alpha = 90°$ for a coated cylinder with $a = 3\lambda_0$, $t_h = 0.06\lambda_0$, $\epsilon_r = 3.25$.

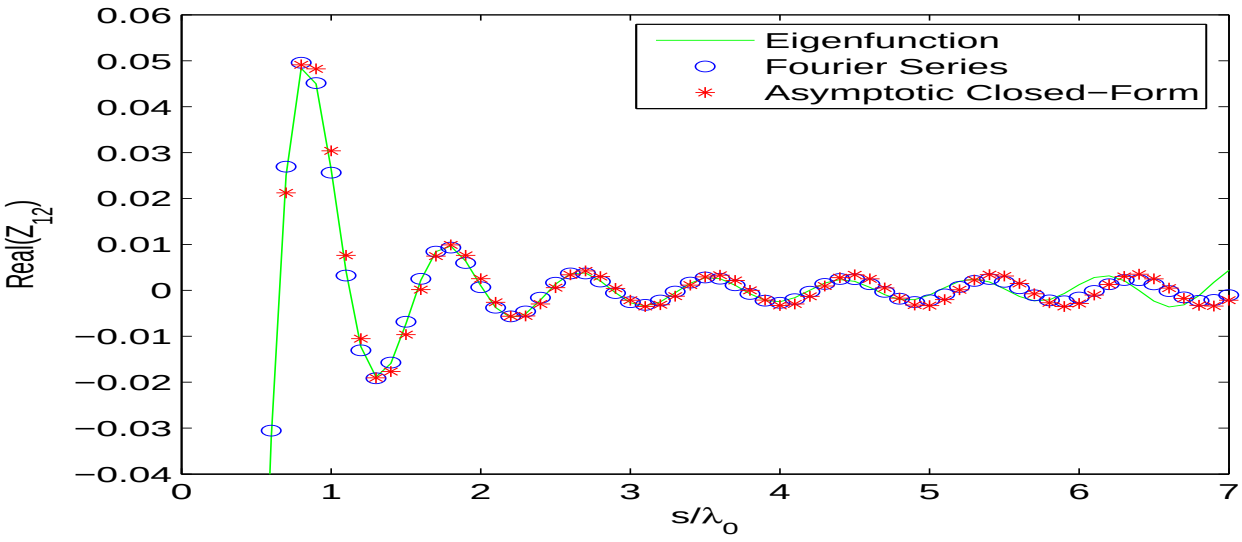


Figure 5.11: Real part of the mutual impedance ($Z_{12}$) between two identical $\hat{\phi}-$directed current sources versus separation $s$ when $\alpha = 70°$ for a coated cylinder with $a = 3\lambda_0$, $t_h = 0.06\lambda_0$, $\epsilon_r = 3.25$.

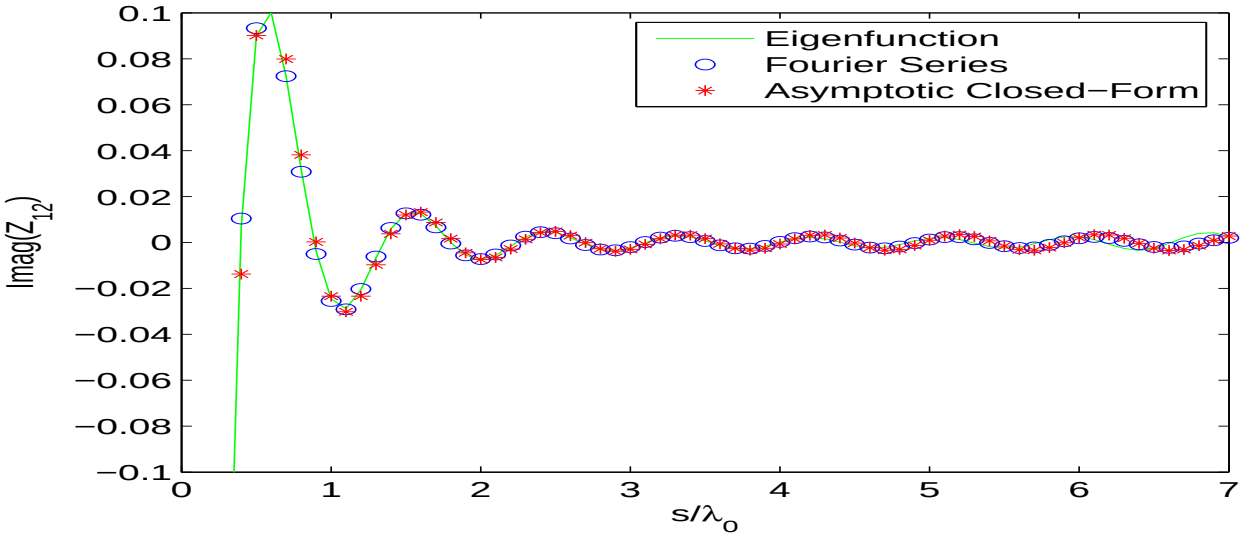


Figure 5.12: Imaginary part of the mutual impedance ($Z_{12}$) between two identical $\hat{\phi}-$directed current sources versus separation $s$ when $\alpha = 70°$ for a coated cylinder with $a = 3\lambda_0$, $t_h = 0.06\lambda_0$, $\epsilon_r = 3.25$.

The table shows that the asymptotic closed-form expressions can be computed faster than the FS expressions by a factor of 100-300 times which is a major advantage. Furthermore, it is known that FS is also 5-6 times faster than the eigenfunction solution [18].

In the figures (5.13) - (5.16), a comparison of effects of $a_{00}$, $a_{01}$, $a_{02}$, $a_{20}$, $a_{21}$, $a_{22}$ parameters on the accuracy of the asymptotic solution is made. In the figures, "Asymptotic 1" is the asymptotic solution where $a_{01} = 0$, $a_{02} = 0$, $a_{21} = 0$ and $a_{22} = 0$, in "Asymptotic 2" $a_{02} = 0$ and $a_{22} = 0$, and "Asymptotic 3" includes all parameters. Mutual coupling between two $\hat{z}$-directed current modes are calculated with $\alpha = 90^\circ$ and $\alpha = 70^\circ$ and other parameters are the same as the previous plots. The plots show that, $a_{00}$, $a_{01}$, $a_{02}$, $a_{20}$, $a_{21}$, $a_{22}$ parameters make the asymptotic solution more accurate at short separations especially for $s < \lambda_0$.

Finally, in the figures (5.17) - (5.20), a parametric study of the asymptotic closed-form expressions are performed. The aim for such a comparison is to recognize the effects of each radius dependent term as well as to distinguish the effects of $f_{a0_Y}(d)$ and $f_{a2_Y}(d)$ separately. In the figures, "Asymptotic 1" is the asymptotic solution where all parameters are included, "Asymptotic 2" is the asymptotic solution where $f_{a2_Y}(d)$ is set to zero, and "Asymptotic 3" the asymptotic solution where $f_{a0_Y}(d)$ is set to zero. These figures show that $f_{a2_Y}(d)$ parameter is absolutely necessary for separations less than $2\lambda_0$ while $f_{a0_Y}(d)$ parameter increases accuracy for separations less than $1\lambda_0$ and for $\alpha \approx 70^\circ$.

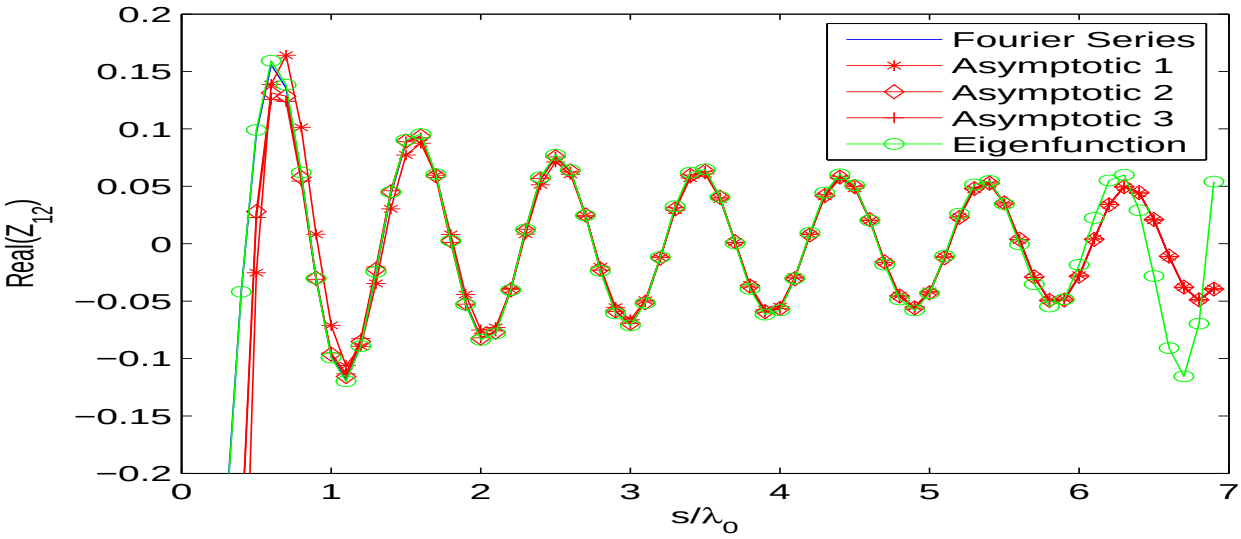


Figure 5.13: Real part of the mutual impedance ($Z_{12}$) between two identical $\hat{z}-$directed current sources versus separation $s$ when $\alpha = 90°$ for a coated cylinder with $a = 3\lambda_0$, $t_h = 0.06\lambda_0$, $\epsilon_r = 3.25$. In "Asymptotic 1", $a_{01} = 0$, $a_{02} = 0$, $a_{21} = 0$ and $a_{22} = 0$, in "Asymptotic 2" $a_{02} = 0$ and $a_{22} = 0$, and in "Asymptotic 3" all parameters are included.

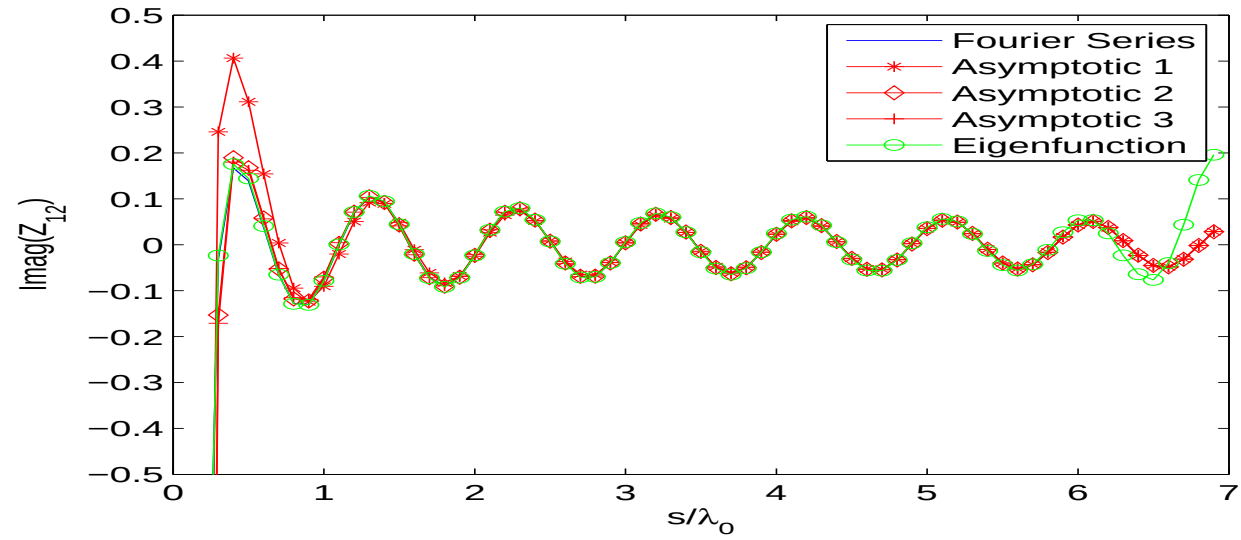


Figure 5.14: Imaginary part of the mutual impedance ($Z_{12}$) between two identical $\hat{z}-$directed current sources versus separation $s$ when $\alpha = 90°$ for a coated cylinder with $a = 3\lambda_0$, $t_h = 0.06\lambda_0$, $\epsilon_r = 3.25$. In "Asymptotic 1", $a_{01} = 0$, $a_{02} = 0$, $a_{21} = 0$ and $a_{22} = 0$, in "Asymptotic 2" $a_{02} = 0$ and $a_{22} = 0$, and in "Asymptotic 3" all parameters are included.

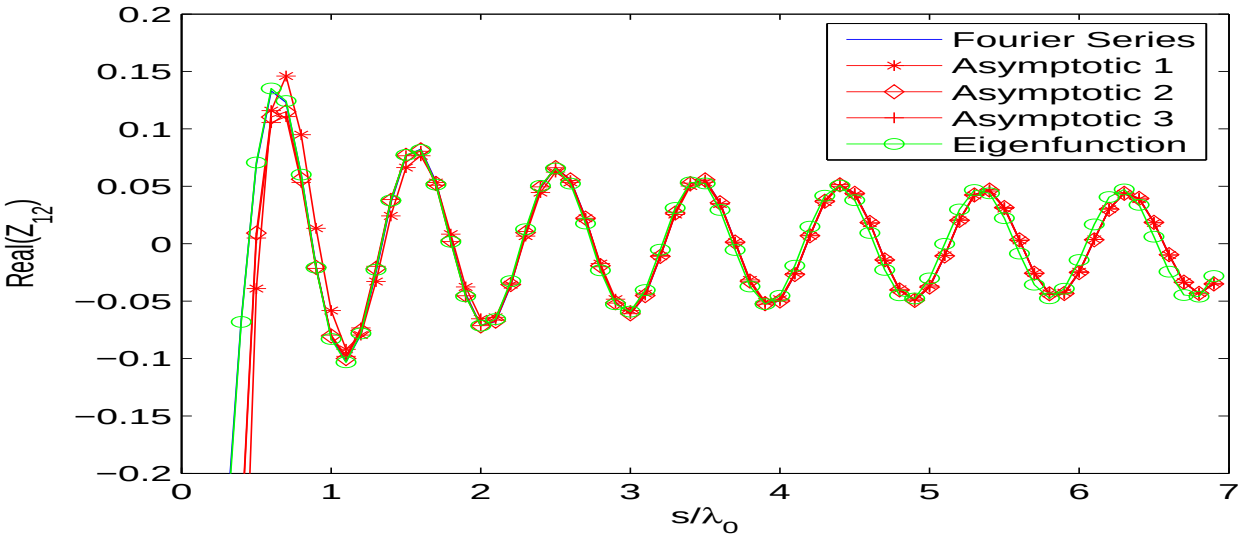


Figure 5.15: Real part of the mutual impedance ($Z_{12}$) between two identical $\hat{z}-$directed current sources versus separation $s$ when $\alpha = 70°$ for a coated cylinder with $a = 3\lambda_0$, $t_h = 0.06\lambda_0$, $\epsilon_r = 3.25$. In "Asymptotic 1", $a_{01} = 0$, $a_{02} = 0$, $a_{21} = 0$ and $a_{22} = 0$, in "Asymptotic 2" $a_{02} = 0$ and $a_{22} = 0$, and in "Asymptotic 3" all parameters are included.

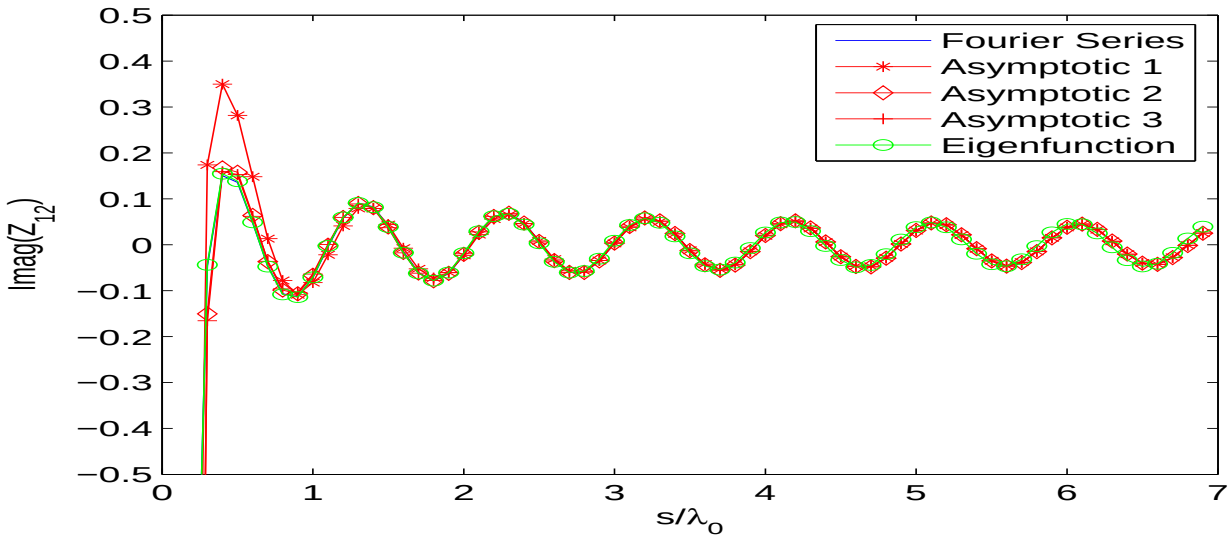


Figure 5.16: Imaginary part of the mutual impedance ($Z_{12}$) between two identical $\hat{z}-$directed current sources versus separation $s$ when $\alpha = 70°$ for a coated cylinder with $a = 3\lambda_0$, $t_h = 0.06\lambda_0$, $\epsilon_r = 3.25$. In "Asymptotic 1", $a_{01} = 0$, $a_{02} = 0$, $a_{21} = 0$ and $a_{22} = 0$, in "Asymptotic 2" $a_{02} = 0$ and $a_{22} = 0$, and in "Asymptotic 3" all parameters are included.

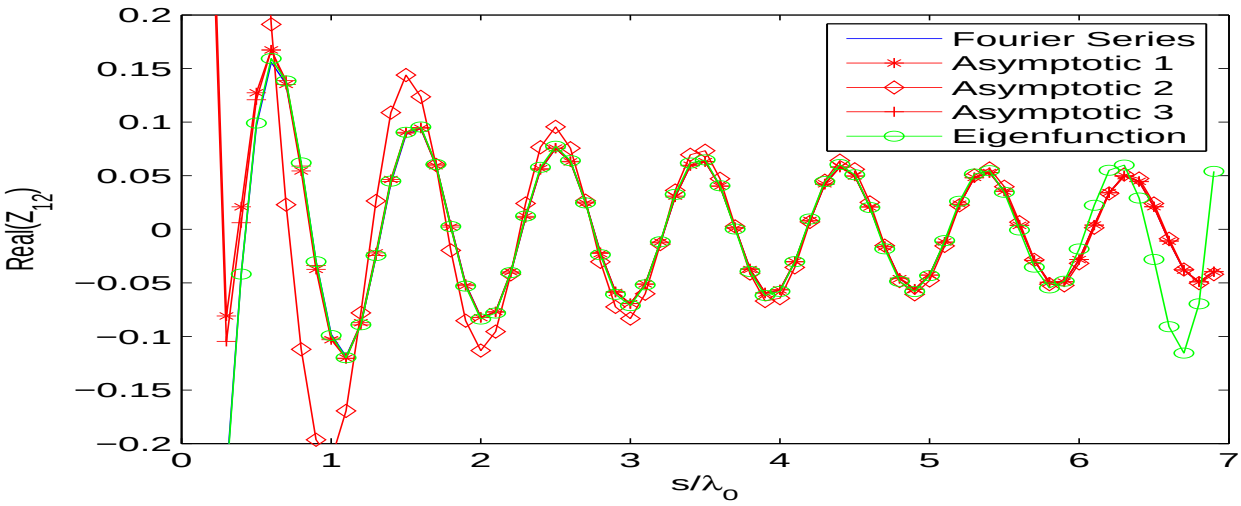


Figure 5.17: Real part of the mutual impedance ($Z_{12}$) between two identical $\hat{z}-$directed current sources versus separation $s$ when $\alpha = 70°$ for a coated cylinder with $a = 3\lambda_0$, $t_h = 0.06\lambda_0$, $\epsilon_r = 3.25$. "Asymptotic 1" is the asymptotic solution where all parameters are included, "Asymptotic 2" is the asymptotic solution where $f_{a2_Y}(d)$ is set to zero, and "Asymptotic 3" the asymptotic solution where $f_{a0_Y}(d)$ is set to zero.

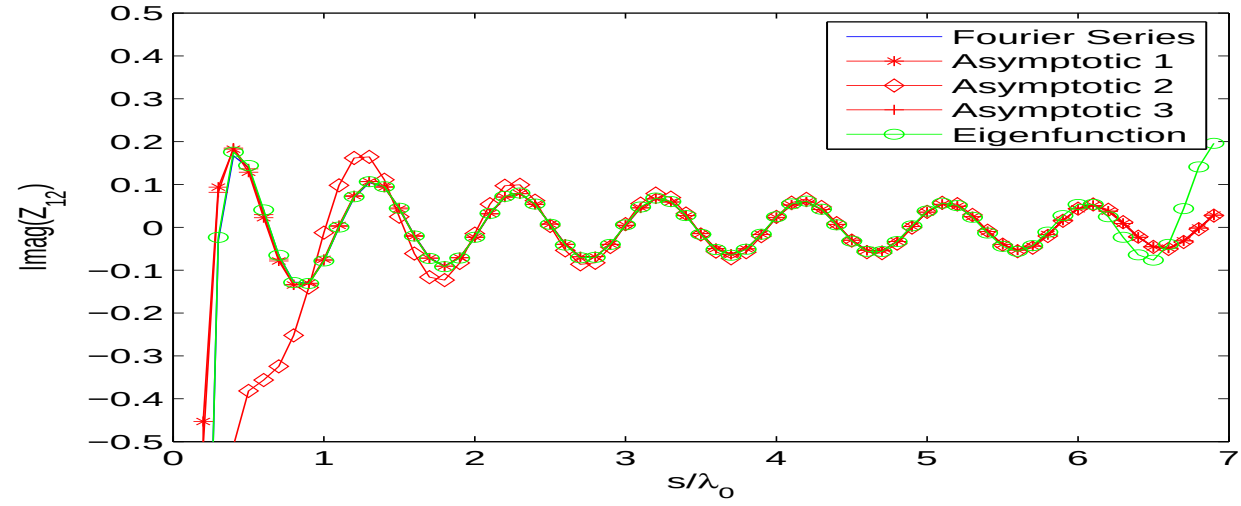


Figure 5.18: Imaginary part of the mutual impedance ($Z_{12}$) between two identical $\hat{z}-$directed current sources versus separation $s$ when $\alpha = 70°$ for a coated cylinder with $a = 3\lambda_0$, $t_h = 0.06\lambda_0$, $\epsilon_r = 3.25$. "Asymptotic 1" is the asymptotic solution where all parameters are included, "Asymptotic 2" is the asymptotic solution where $f_{a2_Y}(d)$ is set to zero, and "Asymptotic 3" the asymptotic solution where $f_{a0_Y}(d)$ is set to zero.

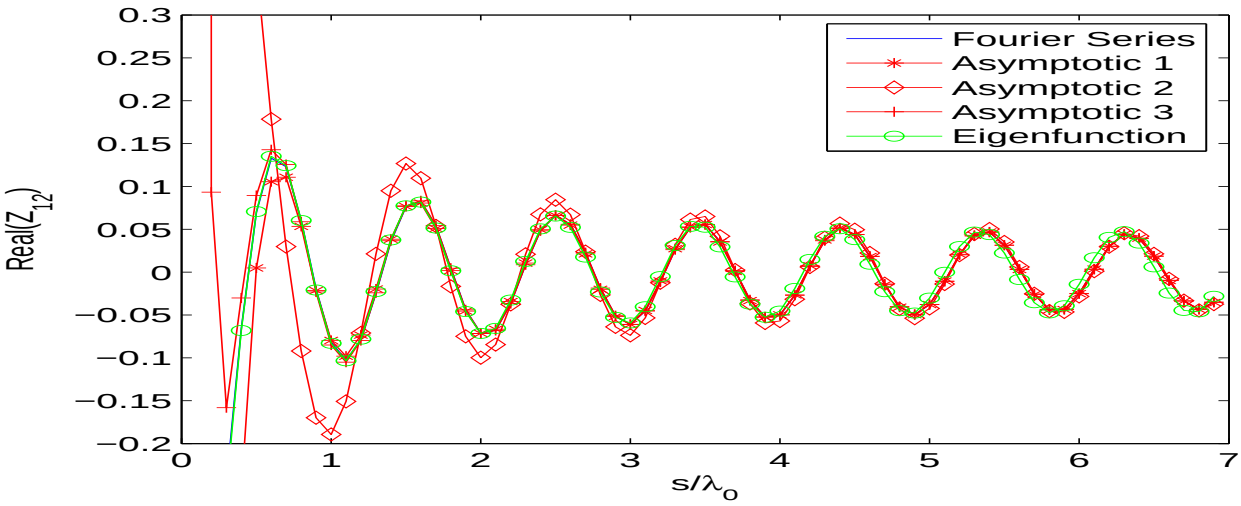


Figure 5.19: Real part of the mutual impedance ($Z_{12}$) between two identical $\hat{z}-$directed current sources versus separation $s$ when $\alpha = 70°$ for a coated cylinder with $a = 3\lambda_0$, $t_h = 0.06\lambda_0$, $\epsilon_r = 3.25$. "Asymptotic 1" is the asymptotic solution where all parameters are included, "Asymptotic 2" is the asymptotic solution where $f_{a2_Y}(d)$ is set to zero, and "Asymptotic 3" the asymptotic solution where $f_{a0_Y}(d)$ is set to zero.

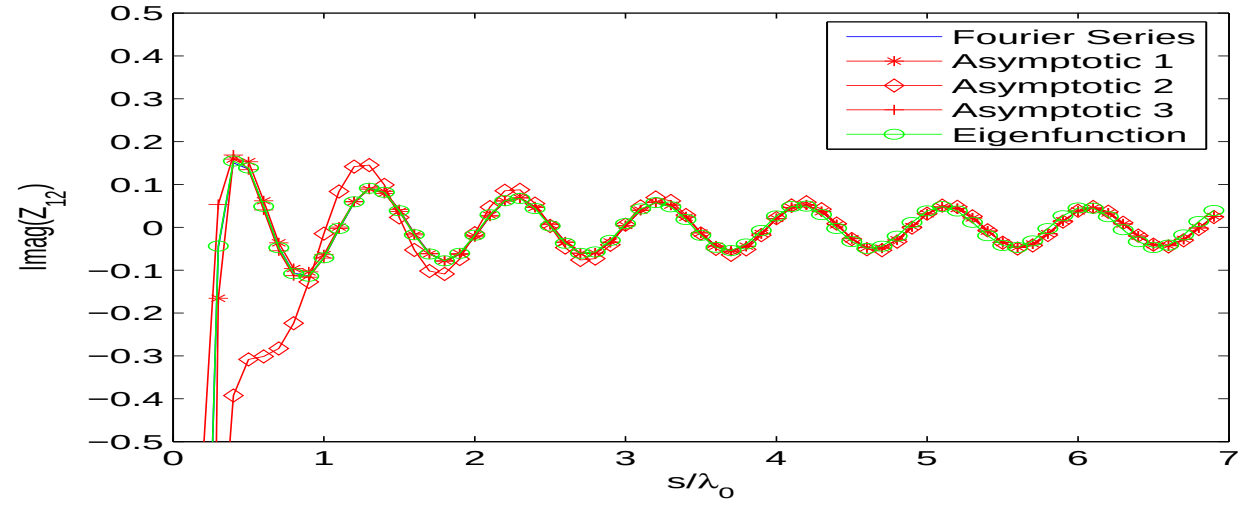


Figure 5.20: Imaginary part of the mutual impedance ($Z_{12}$) between two identical $\hat{z}-$directed current sources versus separation $s$ when $\alpha = 70°$ for a coated cylinder with $a = 3\lambda_0$, $t_h = 0.06\lambda_0$, $\epsilon_r = 3.25$. "Asymptotic 1" is the asymptotic solution where all parameters are included, "Asymptotic 2" is the asymptotic solution where $f_{a2_Y}(d)$ is set to zero, and "Asymptotic 3" the asymptotic solution where $f_{a0_Y}(d)$ is set to zero.

# Chapter 6

# Conclusions

In this dissertation, a relatively simple asymptotic closed-form expressions are developed for surface fields of a dielectric coated PEC circular cylinder. The asymptotic solution is developed on top of the final results of [18] by using the method used in [20]. Therefore, similar to [18], the asymptotic solutions developed in this thesis are valid along the paraxial region. The large parameter in this asymptotic closed-form expressions are the length of geodesic ray connecting the source and observation points. In addition, the cylinder is electrically large enough ($r > \lambda_0$), which has been made use in arriving the final results of [18]. The final expressions developed are relatively simple in mathematical form containing some polynomial and trigonometric functions. They are approximately 100-300 times faster than other available solution techniques (FS and eigenfunction). Furthermore, the derived expressions recover their planar counterparts given in [20] as the inner and outer radii of the cylinder go to infinity while the thickness of the coating remains the same. The accuracy of the proposed method is tested through some mutual coupling calculations between various combinations of $\hat{z}$ and $\hat{\phi}$ directed current modes. The mutual coupling results evaluated using this asymptotic closed-form expressions are compared with the mutual coupling results obtained using the FS solution [18] and the eigenfunction solution. The results show that for the cases simulated, the solutions developed in this thesis provide very accurate results for separations greater than $1\lambda_0$. However, the

method works even for smaller separations for some components. Note that some accuracy problems have been noticed for relatively thin substrates ($t_h < 0.02\lambda_0$) combined with small separations in relatively electrically small cylinders. Furthermore, we observed that the accuracy of this method greatly improves as the radius of the cylinder and the separation between the source and observation points increase. Since the final expressions are in closed-form and can be explained in terms of rays, this technique is very suitable for the development of asymptotic solutions for arbitrarily convex, material coated smooth surfaces.

# Appendix A

# Explicit expressions for the residues of $U$, $V$ and $W$ functions

The explicit expressions for the residues of $U$, $V$ and $W$ functions are given as;

$$R_U(\zeta_p'') = \frac{1}{2}\frac{\zeta_{p''}}{\left[1 - j\frac{\zeta_{p''}}{\alpha_{p''}}(\ cot(t_h\alpha_{p''}) - t_h\alpha_{p''}(1 + \ cot^2(t_h\alpha_{p''})))\right]} \tag{A.1}$$

$$R_V(\zeta_p') = -\frac{1}{2}\frac{\zeta_{p'}^2}{\left[1 + \frac{j\zeta_{p'}}{\epsilon_r\alpha_{p'}}(\ tan(t_h\alpha_{p'}) - t_h\alpha_{p'}(1 + \ tan^2(t_h\alpha_{p'})))\right]} \tag{A.2}$$

$$R_W(\zeta_p'') = \frac{1}{2}\frac{\zeta_{p''}^2}{\left[1 - j\frac{\zeta_{p''}}{\alpha_{p''}}(\ cot(t_h\alpha_{p''}) - t_h\alpha_{p''}(1 + \ cot^2(t_h\alpha_{p''})))\right]}\frac{1}{\zeta_{p''} + \frac{j}{\epsilon_r}\alpha_{p''}\ \ tan(t_h\alpha_{p''})} \tag{A.3}$$

$$R_W(\zeta_p') = \frac{1}{2}\frac{\zeta_{p'}^2}{\left[1 + \frac{j\zeta_{p'}}{\epsilon_r\alpha_{p'}}(\ tan(t_h\alpha_{p'}) + t_h\alpha_{p'}(1 + \ tan^2(t_h\alpha_{p'})))\right]}\frac{1}{\zeta_{p'} - j\alpha_{p'}\ \ cot(t_h\alpha_{p'})} \tag{A.4}$$

and

$$\alpha_{p'} \equiv \sqrt{(\epsilon_r - 1)k_0^2 + \zeta_{p'}^2}; \quad \alpha_{p''} \equiv \sqrt{(\epsilon_r - 1)k_0^2 + \zeta_{p''}^2}; \tag{A.5}$$

# Appendix B

# Formulas for $f_{a0_Y}(d)$ and $f_{a2_Y}(d)$ parameters of special functions

## B.1 Special function P

$$f_{a0_P}(d) = a^p_{0\,0} + \frac{a^p_{0\,1}}{d} + \frac{a^p_{0\,2}}{d^2} \tag{B.1}$$

$$\begin{aligned} a^p_{00} &= 0 && \text{(B.2)} \\ a^p_{01} &= -\frac{tan^3(t_h k_0\sqrt{\epsilon_r - 1})}{2k_0(\epsilon_r - 1)^{3/2}} && \text{(B.3)} \\ a^p_{02} &= -\frac{D_1 + D_2}{4k_0^3 c_o^6(\epsilon_r - 1)^{7/2}} && \text{(B.4)} \end{aligned}$$

where

$$\begin{aligned} D_1 &= k_0\sqrt{\epsilon_r - 1}\,(-6c_o^4\epsilon_r + 3c_o^6\epsilon_r + 3c_o^2\epsilon_r) - (3\epsilon_r - 2)t_h s_i^3 c_o k_0^2 && \text{(B.5)} \\ D_2 &= k_0\sqrt{\epsilon_r - 1}\,[-3t_h^2 c_o^2 s_i^2 k_0^2(\epsilon_r - 1) - 12c_o^2 + 9c_o^4 + 5] + 3t_h c_o k_0^2 s_i^3 && \text{(B.6)} \end{aligned}$$

$$\begin{aligned} c_o &= cos(k_0 t_h\sqrt{\epsilon_r - 1}) && \text{(B.7)} \\ s_i &= sin(k_0 t_h\sqrt{\epsilon_r - 1}) && \text{(B.8)} \end{aligned}$$

and

$$f_{a2_P}(d) = a^p_{2\,0} + \frac{a^p_{2\,1}}{d} + \frac{a^p_{2\,2}}{d^2} \tag{B.9}$$

$$a^p_{2\,0} = \frac{tan^2(t_h k_0\sqrt{\epsilon_r - 1})}{2k_0^2(\epsilon_r - 1)} \tag{B.10}$$

$$a^p_{21} = \frac{(c_o^4 + 2c_o^2[k_0^2 t_h^2(\epsilon_r - 1) - \epsilon_r] + 3c_o k_0 s_i t_h\sqrt{\epsilon_r - 1} - 4 + 5c_o^2)s_i}{2k_0^3 c_o^5(\epsilon_r - 1)^{5/2}} \tag{B.11}$$

$$a^p_{22} = \frac{(B_1 + B_2 + B_3 + B_4 + B_5)}{16k_0^5 c_o^8 s_i(\epsilon_r - 1)^{9/2}} \tag{B.12}$$

where

$$\begin{aligned}
B_1 &= 42 + 25k_0^2 t_h^2 c_o^2(1 - \epsilon_r) - 47k_0^2 t_h^2 c_o^4 + 24k_0^2 t_h^2 c_o^6(\epsilon_r - 1) \\
B_2 &= 6k_0^4 t_h^4 c_o^4(1 - 2\epsilon_r + 6\epsilon_r^2) + 71k_0^2 t_h^2 c_o^4\epsilon_r - 33k_0\sqrt{\epsilon_r - 1}s_i t_h c_o^5 - 60k_0\sqrt{\epsilon_r - 1}s_i t_h c_o \\
B_3 &= k_0\sqrt{\epsilon_r - 1}[24k_0^2 t_h^3 c_o^3 s_i(\epsilon_r - 1) + 12k_0^2 t_h^3 c_o^5 + 93s_i t_h c_o^3] - 108c_o^2 + 6c_o^4\epsilon_r^2 - 84c_o^4\epsilon_r \\
B_4 &= 40c_o^2\epsilon_r + 6c_o^8\epsilon_r^2 + 48c_o^6\epsilon_r - 4c_o^8\epsilon_r - 12c_o^6\epsilon_r^2 + 90c_o^4 - 24c_o^6 - 24k_0\sqrt{\epsilon_r - 1}s_i t_h c_o^3\epsilon_r \\
B_5 &= k_0\sqrt{\epsilon_r - 1}(-12k_0^2 t_h^3 c_o^5 s_i\epsilon_r + 24t_h c_o^5 s_i\epsilon_r) - 24k_0^2 t_h^2 c_o^5\epsilon_r^2
\end{aligned} \tag{B.13}$$

$$c_o = cos(k_0 t_h\sqrt{\epsilon_r - 1}) \tag{B.14}$$

$$s_i = sin(k_0 t_h\sqrt{\epsilon_r - 1}) \tag{B.15}$$

## B.2 Special function Q

$$f_{a0_Q}(d) = a^q_{0\,0} + \frac{a^q_{0\,1}}{d} + \frac{a^q_{0\,2}}{d^2} \tag{B.16}$$

$$a^q_{00} = 0 \tag{B.17}$$

$$a^q_{01} = 0 \tag{B.18}$$

$$a_{02}^{q} \;=\; -\frac{(\epsilon_r^2 - 2\epsilon_r + 4)c_o^4 + 3 - 6c_o^2}{4k_0^2(\epsilon_r - 1)^2 c_o^4} \tag{B.19}$$

$$f_{a2_Q}(d) = a_{2\,0}^{q} + \frac{a_{2\,1}^{q}}{d} + \frac{a_{2\,2}^{q}}{d^2} \tag{B.20}$$

$$a_{20}^{q} \;=\; \frac{1}{2k_0^2} \tag{B.21}$$

$$a_{21}^{q} \;=\; \frac{[\epsilon_r^2 - \epsilon_r - (s_i/c_o)^4]c_o}{2k_0^3 s_i(\epsilon_r - 1)^{3/2}} \tag{B.22}$$

$$a_{22}^{q} \;=\; \frac{(Q_1 + Q_2 + Q_3)}{2k_0^5(\epsilon_r - 1)^{7/2} c_o^6 s_i^2} \tag{B.23}$$

where

$$\begin{aligned}
Q_1 \;&=\; k_0\sqrt{\epsilon_r - 1}\,[10 + 3\epsilon_r c_0^2 + \epsilon_r^2 c_0^6(\epsilon_r - 1) - 9\epsilon_r c_0^4 + 8\epsilon_r c_0^6 + 6k_0^2 t_h^2 c_0^2(1 - \epsilon_r)] \\
Q_2 \;&= k_0\,\sqrt{\epsilon_r - 1}\,(33c_0^4 - 31c_0^2 + 12k_0^2 t_h^2 c_0^4(\epsilon_r - 1)) \\
&\quad -6s_i c_0 t_h k_0^2\,(\epsilon_r - 1 + 2c_0^2) + 12 s_i t_h k_0^2 c_0^3 \epsilon_r \\
Q_3 \;&=\; k_0\,\sqrt{\epsilon_r - 1}\,(-13c_0^8\epsilon_r^3 + 6c_0^8\epsilon_r^4 + 7c_0^8\epsilon_r^2 - 2\epsilon_r c_0^8) \\
&\quad -6k_0^3 t_h^2 c_0^6(\epsilon_r - 1)^{3/2} + 6k_0^2 s_i t_h c_0^5(1 - \epsilon_r)
\end{aligned} \tag{B.24}$$

## B.3 Special function M-R

$$f_{a0_{(M-R)}}(d) = a_{0\,0}^{(m-r)} + \frac{a_{0\,1}^{(m-r)}}{d} + \frac{a_{0\,2}^{(m-r)}}{d^2} \tag{B.25}$$

where

$$a_{00}^{(m-r)} \;= 0 \tag{B.26}$$

$$a_{01}^{(m-r)} \;=\; \frac{0.25(\epsilon_r \;-\; \frac{2}{c_0^2})\;\; tan(t_h k_0\sqrt{\epsilon_r - 1})}{k_0\sqrt{\epsilon_r - 1}} \tag{B.27}$$

$$a_{02}^{(m-r)} = \frac{k_0 t_h D + \sqrt{\epsilon_r - 1}E}{8k_0^2(\epsilon_r - 1)^{3/2}} \tag{B.28}$$

$$D = (2t_g^3 + 2t_g - 2t_g\epsilon_r - 2t_g^5\epsilon_r - 4\epsilon_r t_g^3 + 2t_g^5) \tag{B.29}$$

$$E = 4\epsilon_r^2 + t_g^2(\epsilon_r^2 - 7\epsilon_r + 8) + 6t_g^6 + 13t_g^4 - 3\epsilon_r t_g^4 - 6\epsilon_r + 1 \tag{B.30}$$

$$t_g = tan(t_h k_0 \sqrt{\epsilon_r - 1}) \tag{B.31}$$

and

$$f_{a2_{(M-R)}}(d) = a_{2\,0}^{(m-r)} + \frac{a_{2\,1}^{(m-r)}}{d} + \frac{a_{2\,2}^{(m-r)}}{d^2} \tag{B.32}$$

where

$$a_{20}^{(m-r)} = \frac{tan^2(t_h k_0 \sqrt{\epsilon_r - 1}) - (\epsilon_r - 1)}{2k_0^2(\epsilon_r - 1)} \tag{B.33}$$

$$a_{21}^{(m-r)} = \frac{MR_1 + MR_2 + MR_3}{8k_0^3 \; tan(t_h k_0 \sqrt{\epsilon_r - 1})(\epsilon_r - 1)^{3/2}} \tag{B.34}$$

$$a_{22}^{(m-r)} = \frac{k_0 t_h A + \sqrt{\epsilon_r - 1}(B + k_0^2 t_h^2 C)}{8t_g^2 k_0^4(\epsilon_r - 1)^{5/2}} \tag{B.35}$$

$$MR_1 = -2\epsilon_r^3 + 8\epsilon_r^2 + 4\epsilon_r^2 t_g^2 - 4\epsilon_r \tag{B.36}$$

$$MR_2 = k_0\sqrt{\epsilon_r - 1}\,[-8t_h t_g^3 - 6t_h t_g^5 - 2t_h t_g] + 8t_g^6 + 14t_g^4 + 6t_g^2 \tag{B.37}$$

$$MR_3 = 2k_0\sqrt{\epsilon_r - 1}t_h\epsilon_r t_g\,(1 + t_g^2) - 6\epsilon_r t_g^4 - 9\epsilon_r t_g^2 \tag{B.38}$$

$$A = -2\epsilon_r^3\,(t_g^5 + t_g^3) + \epsilon_r^2\,(28t_g^5 + 16t_g^3 + 12t_g^7) + 89t_g^7 + 36t_g^9 + \epsilon_r(-31t_g^3 - 36t_g^9 - 101t_g^7 - 96t_g^5) + 17t_g^3 + 70t_g^5 \quad \text{(B.39)}$$

$$B = -(30t_g^{10} + t_g^8(84 - 20\epsilon_r) + t_g^6(12\epsilon_r^2 - 54\epsilon_r + 80) - 30\epsilon_r^3 + 12\epsilon_r^4 + t_g^4(32\epsilon_r^2 - 6\epsilon_r^3 + 28 - 50\epsilon_r) + t_g^2(2\epsilon_r^4 - 18\epsilon_r^3 + 2 + 20\epsilon_r^2 - 20\epsilon_r)) \quad \text{(B.40)}$$

$$C = 11\epsilon_r t_g^6 + 5\epsilon_r t_g^8 + \epsilon_r t_g^2 - 7t_g^4 - 11t_g^6 - 5t_g^8 - t_g^2 - 7\epsilon_r t_g^4 \quad \text{(B.41)}$$

$$t_g = tan(t_h k_0 \sqrt{\epsilon_r - 1}) \quad \text{(B.42)}$$

## B.4 Special function S and T

$$f_{a0_S}(d) = 0 \quad \text{(B.43)}$$

$$f_{a2_S}(d) = 0 \quad \text{(B.44)}$$

$$f_{a0_T}(d) = 0 \quad \text{(B.45)}$$

$$f_{a2_T}(d) = 0 \quad \text{(B.46)}$$

# Appendix C

# Explicit expressions for the residues of $P$, $Q$, $M$, $R$, $S$, and $T$ functions

## C.1 Residues for special functions $P$, $Q$, $M$, $R$

$$R_P(\zeta_{p''}) = \frac{1}{2}\frac{\zeta_{p''}}{jD_{Tmp}(\zeta_{p''})} \tag{C.1}$$

$$R_Q(\zeta_{p''}) = \frac{1}{2}\frac{\zeta_{p''}^3}{j(k_0^2-\zeta_{p''}^2)}\frac{\frac{1}{2d}\left(\frac{\epsilon_r(k_0^2-\zeta_{p''}^2)}{A(\zeta_{p''})} - \frac{t_h^2(k_0^2-\zeta_{p''}^2)}{sin^2(t_h\sqrt{A(\zeta_{p''})})} + \frac{k_0^2}{\zeta_{p''}^2}\right) + \frac{(k_0^2-\zeta_{p''}^2)(\epsilon_r-1)}{tan(t_h\sqrt{A(\zeta_{p''})})\sqrt{A(\zeta_{p''})}}}{D_{Tmp}(\zeta_{p''})T_m^0(\zeta_{p''})} \tag{C.2}$$

$$R_Q(\zeta_{p'}) = \frac{1}{2}\frac{\zeta_{p'}^3}{j(k_0^2-\zeta_{p'}^2)}\frac{\frac{1}{2d}\left(\frac{\epsilon_r(k_0^2-\zeta_{p'}^2)}{A(\zeta_{p'})} - \frac{t_h^2(k_0^2-\zeta_{p'}^2)}{sin^2(t_h\sqrt{A(\zeta_{p'})})} + \frac{k_0^2}{\zeta_{p'}^2}\right) + \frac{(k_0^2-\zeta_{p'}^2)(\epsilon_r-1)}{tan(t_h\sqrt{A(\zeta_{p'})})\sqrt{A(\zeta_{p'})}}}{T_m^p(\zeta_{p'})D_{Tm0}(\zeta_{p'})} \tag{C.3}$$

$$R_M(\zeta_{p'}) = \frac{1}{2}\frac{\zeta_{p'}}{jD_{Tm0}(\zeta_{p'})} \tag{C.4}$$

$$R_R(\zeta_{p''}) = \frac{1}{2}\frac{k_0^2(\epsilon_r-1)\zeta_{p''}(-j\zeta_{p''}-\frac{1}{2d})}{jA(\zeta_{p''})D_{Te0}(\zeta_{p''})T_m^0(\zeta_{p''})} \tag{C.5}$$

$$R_R(\zeta_{p'}) = \frac{1}{2}\frac{k_0^2(\epsilon_r-1)\zeta_{p'}(-j\zeta_{p'}-\frac{1}{2d})}{jA(\zeta_{p'})T_e^0(\zeta_{p'})D_{Tm0}(\zeta_{p'})} \tag{C.6}$$

where

$$\begin{aligned} D_{Tmp}(\zeta_{p''}) &= -j - \frac{\zeta_{p''}}{\sqrt{A(\zeta_{p''})}\ tan(t_h\sqrt{A(\zeta_{p''})})} + \frac{t_h\zeta_{p''}}{sin^2(t_h\sqrt{A(\zeta_{p''})})} \\ &+\frac{0.5}{d}\left(\frac{2k_0^2}{\zeta_{p''}^3} - \frac{2\epsilon_r k_0^2\zeta_{p''}}{A^2(\zeta_{p''})} + \frac{2t_h^2\zeta_{p''}}{sin^2(t_h\sqrt{A(\zeta_{p''})})}\right. \\ &\left.+\frac{2t_h^3(k_0^2-\zeta_{p''}^2)\zeta_{p''}}{tan(t_h\sqrt{A(\zeta_{p''})})\ sin^2(t_h\sqrt{A(\zeta_{p''})})\sqrt{A(\zeta_{p''})}}\right) \end{aligned} \tag{C.7}$$

$$\begin{aligned} D_{Tm0}(\zeta_{p'}) &= -j - \frac{2\epsilon_r\zeta_{p'}}{\sqrt{A(\zeta_{p'})}\ tan(t_h\sqrt{A(\zeta_{p'})})} + \frac{\epsilon_r\zeta_{p'}^3}{tan(t_h\sqrt{A(\zeta_{p'})})A^{3/2}(\zeta_{p'})} \\ &+\frac{t_h\zeta_{p'}^3\epsilon_r}{sin^2(t_h\sqrt{A(\zeta_{p'})})A^2(\zeta_{p'})} + \frac{1}{2d}(\frac{2\epsilon_r\zeta_{p'}(1-\zeta_{p'}^2)}{A^2(\zeta_{p'})}) \end{aligned} \tag{C.8}$$

$$\begin{aligned} D_{Te0}(\zeta_{p''}) &= -j + \frac{2\zeta_{p''}}{\sqrt{A(\zeta_{p''})}\ cot(t_h\sqrt{A(\zeta_{p''})})} - \frac{2\zeta_{p''}^3}{A^{3/2}(\zeta_{p''})\ cot(t_h\sqrt{A(\zeta_{p''})})} \\ &-\frac{\zeta_{p''}^2}{A(\zeta_{p''})}(-\frac{\zeta_{p''}}{\sqrt{A(\zeta_{p''})}\ cot(t_h\sqrt{A(\zeta_{p''})})} - \frac{t_h\zeta_{p''}}{cos^2(t_h\sqrt{A(\zeta_{p''})})}) \\ &+\frac{1}{d}\left(\frac{\zeta_{p''}^3\ tan^2(t_h\sqrt{A(\zeta_{p''})})}{A^2(\zeta_{p''})} - \frac{\zeta_{p''}\ tan^2(t_h\sqrt{A(\zeta_{p''})})}{A(\zeta_{p''})}\right. \\ &\left.-\frac{\zeta_{p''}^2\ tan(t_h\sqrt{A(\zeta_{p''})})t_h\zeta_{p''}}{cos^2(t_h\sqrt{A(\zeta_{p''})})A^{3/2}(\zeta_{p''})}\right) \end{aligned} \tag{C.9}$$

$$T_m^p(\zeta_{p'}) = -j\zeta_{p'} - \frac{\sqrt{A(\zeta_{p'})}}{tan(t_h\sqrt{A(\zeta_{p'})})} - \frac{1}{2d}(\frac{k_0^2}{\zeta_{p'}^2} - \frac{\epsilon_r k_0^2}{A(\zeta_{p'})} - \frac{t_h^2(k_0^2-\zeta_{p'}^2)}{sin^2(t_h\sqrt{A(\zeta_{p'})})}) \tag{C.10}$$

$$T_m^0(\zeta_{p''}) = -j\zeta_{p''} - \epsilon_r\frac{\zeta_{p''}^2}{A(\zeta_{p''})}\frac{\sqrt{A(\zeta_{p''})}}{tan(t_h\sqrt{A(\zeta_{p''})})} - \frac{(\epsilon_r-1)\zeta_{p''}^2}{2dA(\zeta_{p''})} \tag{C.11}$$

$$T_e^0(\zeta_{p''}) = -j\zeta_{p''} + \frac{\zeta_{p''}^2}{\sqrt{A(\zeta_{p''})}\ cot(t_h\sqrt{A(\zeta_{p''})})} - \frac{1}{2d}\left(1 + \frac{\zeta_{p''}^2\ tan^2 t_h\sqrt{A(\zeta_{p''})}}{\sqrt{A(\zeta_{p''})}}\right) \tag{C.12}$$

$$A(x) = (\epsilon_r - 1)k_0^2 + x^2 \tag{C.13}$$

## C.2 Residues for special functions $S$ and $T$

$$\begin{aligned} R_S(\zeta_{p''}) &= \left(\frac{\sqrt{A(\zeta_{p''})}}{2\epsilon_r d}\right) \\ &\quad \left\{\frac{Num_1^0(\zeta_{p''})d^2 + Num_2^0(\zeta_{p''})d + A_3^0 T_0^0(\zeta_{p''})}{D_{Pl1p}(\zeta_{p''})Pl_2^{\frac{\pi}{2}}(\zeta_{p''})[T_0^0(\zeta_{p''})d^2 + T_1^0(\zeta_{p''})d + T_2^0(\zeta_{p''})]}\right\} \end{aligned} \tag{C.14}$$

$$\begin{aligned} R_T(\zeta_{p'}) &= \left(\frac{\zeta_{p'}}{2d\sqrt{k_0^2 - \zeta_{p'}^2}}\right) \\ &\quad \left\{\frac{Num_1^{\frac{\pi}{2}}(\zeta_{p'})d^2 + Num_2^{\frac{\pi}{2}}(\zeta_{p'})d + A_3^{\frac{\pi}{2}} T_0^{\frac{\pi}{2}}(\zeta_{p'})}{Pl_1^{\frac{\pi}{2}}(\zeta_{p'})D_{Pl2p}(\zeta_{p'})[T_0^{\frac{\pi}{2}}(\zeta_{p'})d^2 + T_1^{\frac{\pi}{2}}(\zeta_{p'})d + T_2^{\frac{\pi}{2}}(\zeta_{p'})]}\right\} \end{aligned} \tag{C.15}$$

$$\begin{aligned} R_T(\zeta_{p''}) &= \left(\frac{\zeta_{p''}}{2d\sqrt{k_0^2 - \zeta_{p''}^2}}\right) \\ &\quad \left\{\frac{Num_1^{\frac{\pi}{2}}(\zeta_{p''})d^2 + Num_2^{\frac{\pi}{2}}(\zeta_{p''})d + A_3^{\frac{\pi}{2}} T_0^{\frac{\pi}{2}}(\zeta_{p''})}{D_{Pl1p}(\zeta_{p''})Pl_2^{\frac{\pi}{2}}(\zeta_{p''})[T_0^{\frac{\pi}{2}}(\zeta_{p''})d^2 + T_1^{\frac{\pi}{2}}(\zeta_{p''})d + T_2^{\frac{\pi}{2}}(\zeta_{p''})]}\right\} \\ &\quad - \left(\frac{\sqrt{A(\zeta_{p''})}}{2\epsilon_r d\sqrt{k_0^2 - \zeta_{p''}^2}}\right) \\ &\quad \left\{\frac{Num_1^0(\zeta_{p''})d^2 + Num_2^0(\zeta_{p''})d + A_3^0 T_0^0(\zeta_{p''})}{D_{Pl1p}(\zeta_{p''})Pl_2^{\frac{\pi}{2}}(\zeta_{p''})[T_0^0(\zeta_{p''})d^2 + T_1^0(\zeta_{p''})d + T_2^0(\zeta_{p''})]}\right\} \end{aligned} \tag{C.16}$$

where the following functions are used:

$$Num_1^0(x) = A_1^0(x)T_0^0(x) - A_0^0(x)T_1^0(x) \quad \text{(C.17)}$$
$$Num_2^0(x) = A_2^0(x)T_0^0(x) - A_0^0(x)T_2^0(x) \quad \text{(C.18)}$$
$$Num_1^{\frac{\pi}{2}}(x) = A_1^{\frac{\pi}{2}}(x)T_0^{\frac{\pi}{2}}(x) - A_0^{\frac{\pi}{2}}(x)T_1^{\frac{\pi}{2}}(x) \quad \text{(C.19)}$$
$$Num_2^{\frac{\pi}{2}}(x) = A_2^{\frac{\pi}{2}}(x)T_0^{\frac{\pi}{2}}(x) - A_0^{\frac{\pi}{2}}(x)T_2^{\frac{\pi}{2}}(x) \quad \text{(C.20)}$$

$$A_0^0(x) = -jx\ S_1^0(x) \quad \text{(C.21)}$$
$$A_1^0(x) = 0.5\left[jx\ S_2^0(x) - S_1^0(x)\right] \quad \text{(C.22)}$$
$$A_2^0(x) = 0.25\left[jx\ S_3^0(x) + S_2^0(x)\right] \quad \text{(C.23)}$$
$$A_3^0(x) = 0.125 S_3^0(x) \quad \text{(C.24)}$$

$$A_0^{\frac{\pi}{2}}(x) = -jx\ S_1^{\frac{\pi}{2}}(x) \quad \text{(C.25)}$$
$$A_1^{\frac{\pi}{2}}(x) = 0.5\left[jx\ S_2^{\frac{\pi}{2}}(x) - \left(-2dC_{fx}^{\frac{\pi}{2}}(x)\right) S_1^{\frac{\pi}{2}}(x)\right] \quad \text{(C.26)}$$
$$A_2^{\frac{\pi}{2}}(x) = 0.25\left[jx\ S_3^{\frac{\pi}{2}}(x) + \left(-2dC_{fx}^{\frac{\pi}{2}}(x)\right) S_2^{\frac{\pi}{2}}(x)\right] \quad \text{(C.27)}$$
$$A_3^{\frac{\pi}{2}}(x) = 0.125\left(-2dC_{fx}^{\frac{\pi}{2}}(x)\right) S_3^{\frac{\pi}{2}}(x) \quad \text{(C.28)}$$

$$T_0^0(x) = Pl_1^0(x)\ Pl_2^0(x) \quad \text{(C.29)}$$
$$T_1^0(x) = -0.5\left[Pl_1^0(x)\ \tilde{C}_2^0(x) + Pl_2^0(x)\ \tilde{C}_1^0(x)\right] \quad \text{(C.30)}$$
$$T_2^0(x) = 0.25\tilde{C}_1^0(x)\ \tilde{C}_2^0(x) \quad \text{(C.31)}$$

$$T_0^{\frac{\pi}{2}}(x) = Pl_1^{\frac{\pi}{2}}(x)\ Pl_2^{\frac{\pi}{2}}(x) \quad \text{(C.32)}$$
$$T_1^{\frac{\pi}{2}}(x) = -0.5\left[Pl_1^{\frac{\pi}{2}}(x)\ \tilde{C}_2^{\frac{\pi}{2}}(x) + Pl_2^{\frac{\pi}{2}}(x)\ \tilde{C}_1^{\frac{\pi}{2}}(x)\right] \quad \text{(C.33)}$$
$$T_2^{\frac{\pi}{2}}(x) = 0.25\tilde{C}_1^{\frac{\pi}{2}}(x)\ \tilde{C}_2^{\frac{\pi}{2}}(x) \quad \text{(C.34)}$$

$$S_1^0(x) = Pl_1^0(x)\ N_1^0(x) \quad \text{(C.35)}$$
$$S_2^0(x) = \tilde{C}_1^0(x)\ N_1^0(x) + Pl_1^0(x)\ N_2^0(x) \quad \text{(C.36)}$$
$$S_3^0(x) = \tilde{C}_1^0(x)\ N_2^0(x) \quad \text{(C.37)}$$

$$S_1^{\frac{\pi}{2}}(x) = Pl_1^{\frac{\pi}{2}}(x)\ N_1^{\frac{\pi}{2}}(x) \quad \text{(C.38)}$$
$$S_2^{\frac{\pi}{2}}(x) = \tilde{C}_1^{\frac{\pi}{2}}(x)\ N_1^{\frac{\pi}{2}}(x) + Pl_1^{\frac{\pi}{2}}(x)\ N_2^{\frac{\pi}{2}}(x) \quad \text{(C.39)}$$
$$S_3^{\frac{\pi}{2}}(x) = \tilde{C}_1^{\frac{\pi}{2}}(x)\ N_2^{\frac{\pi}{2}}(x) \quad \text{(C.40)}$$

$$N_1^0(x) = \frac{k_0^2}{A(x)} \left( \frac{-\sqrt{A(x)}}{cot\left[t_h\sqrt{A(x)}\right]} \right) \tag{C.41}$$

$$N_2^0(x) = \frac{k_0^2}{A(x)}\ tan^2\left[t_h\sqrt{A(x)}\right] \tag{C.42}$$

$$N_1^{\frac{\pi}{2}}(x) = \frac{1}{\epsilon_r} \left( \frac{-\sqrt{A(x)}}{cot\left[t_h\sqrt{A(x)}\right]} \right) \tag{C.43}$$

$$N_2^{\frac{\pi}{2}}(x) = \frac{t_h^2 k_0^2 - x^2}{\epsilon_r\ cos^2\left[t_h\sqrt{A(x)}\right]} + \frac{k_0^2}{A(x)}\ tan^2\left[t_h\sqrt{A(x)}\right] \tag{C.44}$$

$$Pl_1^0(x) = 1 - \epsilon_r \frac{x^2}{A(x)} \tag{C.45}$$

$$Pl_2^0(x) = 1 + \frac{x^2}{A(x)}\ tan^2\left[t_h\sqrt{A(x)}\right] \tag{C.46}$$

$$Pl_1^{\frac{\pi}{2}}(x) = -jx - \frac{\sqrt{A(x)}}{tan\left[t_h\sqrt{A(x)}\right]} \tag{C.47}$$

$$Pl_2^{\frac{\pi}{2}}(x) = -jx + \frac{1}{\epsilon_r} \left( \frac{\sqrt{A(x)}}{cot\left[t_h\sqrt{A(x)}\right]} \right) \tag{C.48}$$

$$D_{Pl1p}(x) = -j - \frac{x}{\sqrt{A(x)}\ tan\left[t_h\sqrt{A(x)}\right]} + \frac{x\ t_h}{sin^2\left[t_h\sqrt{A(x)}\right]} \tag{C.49}$$

$$D_{Pl2p}(x) = -j + \frac{x}{\epsilon_r\ \sqrt{A(x)}\ cot\left[t_h\sqrt{A(x)}\right]} + \frac{x\ t_h}{\epsilon_r\ cos^2\left[t_h\sqrt{A(x)}\right]} \tag{C.50}$$

$$\tag{C.51}$$

$$\tilde{C}_1^0(x) = -jx - \epsilon_r \left(\frac{x^2}{A(x)}\right) \frac{\sqrt{A(x)}}{tan\left[t_h\sqrt{A(x)}\right]} \tag{C.52}$$

$$\tilde{C}_2^0(x) = -jx + \left(\frac{x^2}{A(x)}\right) \frac{\sqrt{A(x)}}{cot\left[t_h\sqrt{A(x)}\right]} \tag{C.53}$$

$$\tilde{C}_1^{\frac{\pi}{2}}(x) = -2dC_{fx}^{\frac{\pi}{2}}(x) - \left(\frac{\epsilon_r k_0^2}{A(x)} - \frac{t_h^2 k_0^2 - x^2}{sin^2\left[t_h\sqrt{A(x)}\right]}\right) \tag{C.54}$$

$$\begin{aligned}\tilde{C}_2^{\frac{\pi}{2}}(x) &= -2dC_{fx}^{\frac{\pi}{2}}(x) \\ &+ \frac{t_h^2 k_0^2 - x^2}{\epsilon_r\ cos^2\left[t_h\sqrt{A(x)}\right]} + \frac{k_0^2}{A(x)}\ tan^2\left[t_h\sqrt{A(x)}\right]\end{aligned} \tag{C.55}$$

and

$$C_{fx}^{\frac{\pi}{2}}(x) = \begin{cases} jx + k_0 \frac{H_{(\sqrt{k_0^2-x^2}d)}^{(2)'}(k_0 d)}{H_{(\sqrt{k_0^2-x^2}d)}^{(2)}(k_0 d)} & |\frac{\sqrt{k_0^2-x^2}}{k_0} - 1| \leq \frac{1}{d^{2/3}} \\ -\frac{1}{2d}\frac{k_0^2}{(x^2)} & \text{elsewhere.} \end{cases} \tag{C.56}$$

$$A(x) = (\epsilon_r - 1)k_0^2 + x^2 \tag{C.57}$$

# Bibliography


[1] A. Nakatini, N. G. Alexopoulus, N. K. Uzunoglu, and P. L. E. Uslenghi, "Accurate Green's function computation for printed circuit antennas on cylindrical antennas", *Electromagn.*, Vol.6, pp. 243-254, July-Sept. 1986.

[2] T. M. Habashy, S. M. Ali and J. A. Kong, "Input impedance and radiation pattern of cylindrical-rectangular and wraparound microstrip antennas", *IEEE Trans. Antennas Propagat.*, Vol.38, pp. 722-731, May 1990.

[3] K. Naishadham, and L. B. Felsen, "Dispersion of waves guided along a cylindrical substrate-superstrate layered medium", *IEEE Trans. Antennas Propagat.*, Vol.41, pp. 304-313, March 1993.

[4] L. W. Pearson, "A construction of the fields radiated by a z-directed point sources of current in the presence of a cylindrically layered obstacle", *Radio Sci.*, Vol.21, pp. 559-569, July-August 1986.

[5] K. -L. Wong, *Design of Nonplanar Microstrip Antennas and Transmission Lines.*, New York: Wiley, 1999.

[6] P. Munk, *A uniform geometrical theory of diffraction for the radiation and mutual coupling associated with antennas on a material coated convex conducting surface,*, PhD thesis, The Ohio-State University Dept. of Electrical Engineering, 1996.

[7] R. G. Rojas and V. B. Ertürk, "UTD ray analysis of mutual coupling and radiation for antennas mounted on dielectric coated PEC convex surfaces", *Proceedings of URSI Int. Symposium on Electromagnetic Theory*, Vol.1, pp. 178-180, May 1998 pp. 1525-1528, July 1998.

[8] V. B. Ertürk and R. G. Rojas, "Efficient computation of surface fields excited on a dielectric coated circular cylinder", *IEEE Trans. Antennas Propagat.*, Vol.48, No. 10, pp. 1507-1516, October 2000.

[9] C. Demirdag, and R. G. Rojas, "Mutual coupling calculations on a dielectric coated PEC cylinder using UTD-based Green's function", *Proc. IEEE Trans. Antennas Propagat. Symp. Dig.*, Vol.3, Montreal, Canada, July 1997, pp. 1525-1528,

[10] M. Marin, and P. Pathak, "Calculation of Surface Fields Created by a Current Distribution on a Coated Circular Cylinder", The Ohio State Univ. ElectrSci. Lab. Dept. Elect. Eng., 721565-1, 1989.

[11] Z. W. Chang, L. B. Felsen and A Hessel, "Surface ray methods for mutual coupling in conformal arrays on cylinder and conical surfaces", Polytech. Inst. New York, Final Rep., 1976 (prepared under contract N00123-76-C-0236).

[12] S. W. Lee, and S. Safavi-Naini, "Asymptotic Solution of Surface Field Due to a Magnetic Dipole on a Cylinder", Univ. Illunois at Urbana-Champaign, Vol.3, Dept.Elec.Eng., 76-11, 1976.

[13] P.H. Pathak and N. Wang, "An analysis of the mutual coupling between antennas on a smooth convex surface", Tech. Rep. 784538-7, The Ohio-State University ElectroScience Lab. Dept. of Electrical Engineering, October 1978.

[14] J. Boersma and S. W. Lee, "Surface field due to a magnetic dipole on a cylinder: asymptotic expansion of exact solution", Univ. Illinois at Urbana Champaign, Dep. Elec. Eng., Electromagn. Lab. Rep. 78-17, 1978

[15] R. J. Pogorzelski, "On the high-frequency asymptotic evaluation of the potentials of elemental sources on an anisotropic impedance cylinder", *Radio Sci.*, Vol.31, pp. 389-399, March-April 1996.

[16] M. Abramowitz, and I. A. Stegun, *Handbook of Mathematical Functions*, New York: Dover, 1970.

[17] V. B. Ertürk, "Efficient Hybrid Mom/Green's Function Technique to Analyze Conformal Microstrip Antennas and Arrays", Ph. D. dissertation, The Ohio State Univ. ElectrSci. Lab. Dept. Elect. Eng., 2000.

[18] V. B. Ertürk and R. G. Rojas, "Paraxial space-domain formulation for surface fields on a large dielectric coated circular cylinder", *IEEE Trans. Antennas Propagat.*, Vol.50, No. 11, pp. 1577-1587, November 2002.

[19] C. Tokgoz, P. H. Pathak and R. J. Marhefka, "An asymptotic solution for the surface magnetic field within the paraxial region of a circular cylinder with an impedance boundary condition", *IEEE Trans. Antennas Propagat.*, Vol.53, No.4, pp. 1435-1443, April 2005.

[20] S. Barkeshli, P. H. Pathak and M. Marin, "An asymptotic closed-form microstrip Green's function for the efficient moment method analysis of mutual coupling in microstrip antennas", *IEEE Trans. Antennas Propagat.*, Vol.38, pp. 1374-1383, September 1990.

[21] M. Marin, S. Barkeshli, and P. Pathak, "On the location of and proper and improper surface wave poles for the grounded dielectric slab", *IEEE Trans. Antennas Propagat.*, Vol.38, pp. 570-573, Apr. 1990.

[22] L. B. Felsen and N. Marcuvitz, *Radiation and Scattering of Waves.*, New Jersey: Prentice-Hall Inc., 1973.

[23] S. Barkeshli, *An efficient approach for evaluating the planar microstrip Green's function and its applications to the analysis of microstrip antennas and arrays,*, PhD dissertation, The Ohio-State University Dept. of Electrical Engineering, Columbus, OH, 1988.

[24] D. M. Pozar, "Input impedance and mutual coupling of rectangular microstrip antennas", *IEEE Trans. Antennas Propagat.*, Vol.30, no. 6, pp. 1191-1196, Nov. 1982.